INTERNATIONAL JOURNAL FOR NUMERICAL METHODS IN FLUIDS
Int. J. Numer. Meth. Fluids **28**: 1441–1479 (1998)

SIMULATION OF GAS–SOLID PARTICLE FLOWS OVER A WIDE RANGE OF CONCENTRATION

CHRISTIAN MASSON[a,*] AND B. RABI BALIGA[b]

[a] *École de Technologie Supérieure, Département de Génie Mécanique, 1100 Notre-Dame, Ouest Montréal, Québec H3C 1K3, Canada*
[b] *McGill University, Department of Mechanical Engineering, 817 Sherbrooke St. W, Montréal, Québec H3A 2K6, Canada*

SUMMARY

A two-fluid model of gas–solid particle flows that is valid for a wide range of the solid-phase volume concentration (dilute to dense) is presented. The governing equations of the fluid phase are obtained by volume averaging the Navier–Stokes equations for an incompressible fluid. The solid-phase macroscopic equations are derived using an approach that is based on the kinetic theory of dense gases. This approach accounts for particle–particle collisions. The model is implemented in a control-volume finite element method for simulations of the flows of interest in two-dimensional, planar or axisymmetric, domains. The chosen mathematical model and the proposed numerical method are applied to three test problems and one demonstration problem. © 1998 John Wiley & Sons, Ltd.

KEY WORDS: gas–solid particle flow; dilute to dense concentrations; two-fluid model; kinetic theory; control-volume finite element method

1. INTRODUCTION

In *dilute* gas–solid particle flows, the motion of the particles is mainly determined by the aerodynamic forces that they experience, and the influence of particle–particle collisions may be assumed to be relatively negligible. In contrast, the particle motion in *dense* gas–solid particle flows is primarily controlled by particle–particle collisions, and the aerodynamic forces on the particles have a relatively negligible influence on their trajectories. Discussions of *dilute* gas–solid particle flows, including quantitative qualification criteria, are available in the works of Crowe [1,2] and Ishii *et al.* [3]. The modelling of *dense* gas–solid particle flows, such as granular flows and fluidized bed flows, have been discussed by Campbell [4], Savage [5] and Gidaspow [6]. Discussions of gas–solid particle flows and related modelling issues, are also available in the works of Jackson [7], Soo [8], Marble [9], Whitaker [10], Ishii [11], Slattery [12], Bouré and Delhaye [13], Drew and Lahey [14], Sirignano [15], Walton [16], Pita and Sundaresan [17,18], and Yasuna *et al.* [19].

Most of the available models of gas–solid particles flows are applicable to either the dilute or the dense regimes of the solid-phase volume concentration. The objectives of this paper are

* Correspondence to: École de Technologie Supérieure, Département de Génie Mécanique, 1100 rue Notre-Dame Ouest, Montréal, Québec H3C 1K3, Canada. Tel: +1 514 3968504; Fax: +1 514 3968530; E-mail: cmasson@mec.etsmtl.ca

CCC 0271–2091/98/201441–39$17.50

Received 12 March 1996
Revised 17 February 1998

to present a *two-fluid* model of gas–solid particle flows that is applicable to a wide range of the solid-phase volume concentration (*dilute to dense*), concisely describe the implementation of this model in a control-volume-based finite element method (CVFEM), and demonstrate the capabilities of the model by applying it to some test and demonstration problems. The two-fluid model presented in this paper is a simplified version of a model proposed by Savage and co-workers [5].

The most detailed model for gas–solid particle flows is the so-called complete local description or exact formulation [13,14,20,21]. This approach deals with the dynamics of each phase and the interface on the basis of first principles. In each phase, the appropriate governing equations are solved, and kinematic and dynamic balance equations are imposed at the interface. Such a complete local description *exactly* models the flow of interest. However, simulations that are based on such complete local descriptions place enormous demands on computational resources [2]. Therefore, some simplifications are essential to obtain models that are tenable for practical simulations of gas–solid particle flows.

Practical models of gas–solid particle flows are obtained by introducing the notion of volume concentration in the context of superimposed continua: each phase is treated as a continuum, simultaneously occupying the same region in space. Rigorous derivations of such models are based on averaging procedures. The early works in averaging theories, such as those of Anderson and Jackson [22], Murray [23], Panton [24], and Buyevich [25], are related to applications involving gas–solid particle flows. The works of Slattery [26] and Whitaker [27] pertain to flows in porous media and are based on the techniques of volume averaging. Averaging formulations for more general multiphase systems can be found in the works of Ishii [11], Bouré and Delhaye [13], Drew, Drew and Lahey [14], [28], Crapiste *et al.* [29], and Jiang *et al.* [30].

Computer simulations of *dilute* gas–solid flows can be done by using either a Lagrangian or Eulerian description for the solid phase. A Eulerian description, typically based on a volume-averaged continuum formulation, is used to model the fluid phase. When the Lagrangian description of the solid phase is used, the effects of the solid phase appear as implied sources of mass, momentum, and energy in the continuum description of the fluid phase. A popular scheme using the Lagrangian description of the solid phase and the implied-source concept is the PSI-CELL model first proposed by Crowe *et al.* [31]. Numerical models of dilute gas–solid particle flows that are based on Eulerian descriptions of both the particles and the fluid employ volume-averaged formulations to model both phases. Such models are often referred to as two-fluid models, and examples of their use can be found in the works of DiGiacinto *et al.* [32], Durst *et al.* [33], Carver [34], Harlow and Amsden [35], and Spalding [36].

Eulerian–Lagrangian descriptions of dilute gas–solid particle flows involve the solution of the equations of motion of a large number of particles. In such formulations, the handling of boundary conditions, though quite demanding computationally, is straightforward once the wall–particle collision properties are known. They can also handle polydispersed particle size distribution [33] more efficiently than the Eulerian–Eulerian formulations. However, the volume concentration of the solid particles does not appear directly in the Eulerian–Lagrangian formulations. Therefore, special treatments are essential [37] to calculate this variable, which appears in the Eulerian description of the fluid phase, and such treatments can adversely affect the effectiveness of the overall solution procedure at high solid-phase volume concentrations. It has also been observed that the Eulerian–Eulerian formulation often converges more easily at high loading than the Eulerian–Lagrangian model, as has been discussed by Durst *et al.* [33]. Furthermore, particle–particle collisions are difficult to take into account in the Eulerian–Lagrangian formulation.

As the solid–particle volume concentration increases, in addition to the interaction between the fluid and the particles, particle–particle interactions must be taken into account. Savage and co-workers (see Reference [5]) have used averaging techniques and concepts similar to those employed in the kinetic theory of dense gases [38] to propose macroscopic mathematical models of dry granular materials (collection of discrete solid particles with no interstitial fluid). There have also been efforts to modify the dry granular flow models to include the effects of the interstitial fluid. Sinclair and Jackson [39] have used such a modification to analyze fully developed gas–solid particle flow in a pipe. In their model, the effects of the fluid are modelled through a drag force appearing in the solid- and fluid-phase momentum equations, and the solid-phase constitutive equations are based on the dry granular flow kinetic theory of Lun *et al*. [40]. A similar model has been developed by Ding and Gidaspow [41] and applied to fluidized beds. Lun and Savage [5,42] have rigorously developed a kinetic theory for gas–solid particle mixtures. Their model is also valid for a wide range of the solid-phase volume concentration. A simplified version of their model is used in this paper and described in the next section.

The granular-temperature models and numerical simulations of Johnson and Jackson [43], Nott and Brady [44], and Sinclair and Jackson [39] are examples of Eulerian–Eulerian descriptions of dense gas–solid particle flows. These numerical simulations are based on one-dimensional formulations. In the work of Ding and Gidaspow [41], multidimensional numerical simulations of high-concentration gas–solid particle flows have been presented. Their numerical solution method uses a staggered-grid finite volume formulation based on the ICE algorithm developed by Harlow and Amsden [35].

Most of the aforementioned numerical simulations of gas–solid particle flows are based on finite difference methods (FDMs) or finite volume methods (FVMs) that use orthogonal line-by-line staggered-grid arrangements for the velocity components and pressure [45]. These methods are best suited for the modelling of such flows in regular-shaped calculation domains. General orthogonal and non-orthogonal boundary-fitted grids can be used to extend their applicability to irregular geometries. However, methods based on finite element discretizations are better suited for the solution of fluid flow problems in complex irregular domains. Recently, a co-located, equal-order CVFEM formulated for the solution of a two-fluid model of *dilute* gas–solid particle flows has been proposed by Masson and Baliga [46–48]. The numerical method proposed in this paper is a CVFEM that is designed to solve two-fluid models of gas–solid particle flows over a wide range of the solid-phase volume concentration in complex two-dimensional planar and axisymmetric domains.

2. MATHEMATICAL MODEL

As was noted in the previous section, several derivations of the governing and constitutive equations of dilute and dense gas-solid particle flows are available in the literature. Lun and Savage [5,42] have proposed perhaps the first model of fluid–solid particle flows that is appropriate for a wide range of the volume concentration of the solid phase, from the *dilute to the dense* regimes. This model uses the so-called granular-temperature concept [5,40].

In the model of Lun and Savage [5,42], the motion of the particles in a gas–solid particle flow are assumed to be analogous to the random motion of the molecules of a gas. Therefore, a macroscopic description of the solid-particle phase can be obtained following procedures akin to those employed in the kinetic theory of dense gases [38]. This model is based on the prescription of a velocity distribution function that is governed by the Boltzmann equation, in

which the external forces applied to the particles and a collisional term appear. The collisional term models the direct particle–particle interactions, using the assumption of binary encounters of inelastic hard spheres, and the contribution of collisions between solid particles and fluid molecules, based on the Fokker–Planck or soft collisional term [5,38,42]. Using an ensemble averaging procedure, the governing equations of the solid-particle phase are obtained along with their accompanying constitutive relations. These constitutive relations involve the granular temperature [5,40] which is a measure of the fluctuating kinetic energy of the solid particles. The motion of the Newtonian fluid phase is governed by the Navier–Stokes equations, which must be satisfied at each point of the continuous phase: appropriate boundary conditions at the domain boundaries and the interface between the particles and the fluid phase complete the mathematical description. However, as was mentioned earlier, for a large number of particles this exact topology is far too complex to allow practical simulations based on such a complete local description of the fluid-phase governing equations. To simplify the description, point variables which vary rapidly on the scale of the particle spacing are volume averaged [22] over regions that are large compared with this spacing, but small compared with the domain of interest. The resulting model [5,42] describes the fluid and solid phases as two interpenetrating continua.

A simplified version of the model of Lun and Savage [5,42] is used in this paper. The interested reader is referred to Reference [49] for a detailed derivation of the governing equations and the constitutive relations. This mathematical model is based on the following assumptions: the solid phase is composed of hard, spherical, smooth, and elastic or slightly inelastic particles of uniform diameter, d; particle–particle interactions through sliding contact, which can occur in situations close to maximum packing, are considered negligible or not allowed; the particles do not coalesce or break up; the mass density of the particles, ρ^{s}, is much larger than the fluid-phase mass density, ρ^{f}; rotation of the particles is neglected; the fluid is Newtonian and incompressible; and the flow of the *fluid* phase is governed by the Navier–Stokes equations, prior to the aforementioned volume-averaging procedure. Furthermore, the model does not allow phase change and chemical reactions, and attention in the paper is limited to two-dimensional, planar or axisymmetric flows. Note that this simplified model is unable to handle regions where there are no solid particles, and it is unsuitable for problems in which there is a smooth transition to the packed-bed state.

2.1. Governing equations

The proposed mathematical model consists of a set of seven differential equations: a continuity equation and two momentum equations for each of the two phases, and a fluctuating kinetic energy equation for the solid phase. The seven dependent variables are u^{f}, v^{f}, p^{f}, u^{s}, v^{s}, α and T. The superscripts f and s refer to the gas (fluid) and particulate (solid particle) phases, respectively. The volume concentration of the solid phase is denoted by α. The volume concentration of the fluid phase, ϵ, is related to α by $\alpha+\epsilon=1$. T is the granular temperature [5,42].

With respect to the cylindrical co-ordinate system (r, θ, z), two-dimensional axisymmetric gas–solid particle flows can be represented by

$$\frac{\partial}{\partial t}(\beta\rho\phi)+\frac{\partial}{\partial z}(\beta\rho u\phi)+\frac{1}{r}\frac{\partial}{\partial r}(r\beta\rho v\phi)=\frac{\partial}{\partial z}\left(\Gamma_{e}\frac{\partial\phi}{\partial z}\right)+\frac{1}{r}\frac{\partial}{\partial r}\left(r\Gamma_{e}\frac{\partial\phi}{\partial r}\right)+S_{\phi}. \tag{1}$$

The appropriate governing equations can be obtained from Equation (1) by defining the dependent variable ϕ, the volume concentration β, the effective diffusion coefficient Γ_{e}, the

mass density ρ, the z-component of velocity u, the r-component of velocity v, and the volumetric source term S_ϕ, according to Table I, where

$$S_{\Gamma z} = \frac{\partial}{\partial z}\left(\Gamma_e \frac{\partial u}{\partial z} + \left(\Gamma_b - \frac{2}{3}\Gamma_e\right)\left(\frac{\partial u}{\partial z} + \frac{1}{r}\frac{\partial}{\partial r}(rv)\right)\right) + \frac{1}{r}\frac{\partial}{\partial r}\left(r\Gamma_e \frac{\partial v}{\partial z}\right), \tag{2}$$

$$S_{\Gamma r} = \frac{\partial}{\partial z}\left(\Gamma_e \frac{\partial u}{\partial r}\right) + \frac{1}{r}\frac{\partial}{\partial r}\left(r\left(\Gamma_e \frac{\partial v}{\partial r} + \left(\Gamma_b - \frac{2}{3}\Gamma_e\right)\left(\frac{\partial u}{\partial z} + \frac{1}{r}\frac{\partial}{\partial r}(rv)\right)\right)\right), \tag{3}$$

$$S_{\text{cyl}} = -\frac{(\Gamma_b - \frac{2}{3}\Gamma_e)(\partial u/\partial z + (1/r)(\partial/\partial r)(rv))}{r} - 2\Gamma_e \frac{v}{r^2}, \tag{4}$$

$$S_{Dz} = \alpha \rho^s \zeta_D (u^f - u^s), \tag{5}$$

$$S_{Dr} = \alpha \rho^s \zeta_D (v^f - v^s), \tag{6}$$

$$S_\alpha = \frac{\partial}{\partial z}\left(k_\alpha^s \frac{\partial \alpha}{\partial z}\right) + \frac{1}{r}\frac{\partial}{\partial r}\left(rk_\alpha^s \frac{\partial \alpha}{\partial r}\right), \tag{7}$$

$$W_p = -p^s\left(\frac{\partial u^s}{\partial z} + \frac{1}{r}\frac{\partial}{\partial r}(rv^s)\right). \tag{8}$$

The terms $S_{\Gamma z}$ and $S_{\Gamma r}$ will be denoted as the *diffusion-source terms*, and Γ_b that appears in the expressions for these terms is a bulk diffusion coefficient: the definitions of Γ_b for the dependent variables of interest are given in Table I. Expressions for the other coefficients and parameters in Equations (1)–(8) are given in the following subsection.

Equations (1)–(8) can be used to model two-dimensional problems formulated in the cylindrical *and* Cartesian co-ordinate systems. To facilitate this general approach to the problem, the terms directly related to the use of the cylindrical co-ordinate system are regrouped in the source term S_{cyl}. This regroupment has been carried out only to emphasize the difference between the cylindrical and Cartesian formulations. In the Cartesian (x, y) formulation, the following specializations are involved: $S_{\text{cyl}} = 0$; in all derivatives $x \equiv z$ and $y \equiv r$; and, then, r is set equal to unity. The source terms S_{Dz} and S_{Dr} are the mutual z- and r-direction drag forces per unit volume of the mixture, respectively, exerted by the fluid and

Table I. Specific forms of the general equation

	β	ρ	u	v	Γ_e	Γ_b	ϕ	S_ϕ
Fluid phase								
z-momentum	ϵ	ρ^f	u^f	v^f	μ_e^f	μ_b^f	u^f	$S_{\Gamma z} - S_{Dz} + S_z^f - \epsilon \frac{\partial p^f}{\partial z}$
r-momentum	ϵ	ρ^f	u^f	v^f	μ_e^f	μ_b^f	v^f	$S_{\Gamma r} - S_{Dr} + S_r^f - \epsilon \frac{\partial p^f}{\partial r} + S_{\text{cyl}}$
Continuity	ϵ	ρ^f	u^f	v^f	0	0	1	0
Solid phase								
Granular temperature	α	$3/2\rho^s$	u^s	v^s	k_T^s	–	T	$W_p + S_\alpha + \Phi^s - \gamma_c - \gamma_D + \gamma_B$
z-momentum	α	ρ^s	u^s	v^s	μ_e^s	μ_b^s	u^s	$S_{\Gamma z} + S_{Dz} + S_z^s - \alpha \frac{\partial p^f}{\partial z} - \frac{\partial p^s}{\partial z}$
r-momentum	α	ρ^s	u^s	v^s	μ_e^s	μ_b^s	v^s	$S_{\Gamma r} + S_{Dr} + S_r^s - \alpha \frac{\partial p^f}{\partial r} - \frac{\partial p^s}{\partial r} + S_{\text{cyl}}$
Continuity	α	ρ^s	u^s	v^s	0	0	1	0

solid phases on one another. Therefore, these source terms will be referred to as the *momentum coupling terms*. S_α represents the rate of transport of solid-phase fluctuating kinetic energy per unit volume because of concentration gradients, and W_p is the rate of work done per unit volume by the solid-phase pressure.

2.2. Constitutive equations

2.2.1. Solid phase.

$$\zeta_{\mathrm{D}} = \frac{3}{4}\frac{\mu^{\mathrm{f}}}{\rho^{\mathrm{s}} d^2} C_{\mathrm{D}} Re^{\mathrm{s}}, \tag{9}$$

$$\gamma_{\mathrm{c}} = 48\eta(1-\eta)\frac{\alpha^2 \rho^{\mathrm{s}} g_0}{d}\left(\frac{T}{\pi}\right)^{1/2} T; \qquad \gamma_{\mathrm{D}} = 3\alpha\rho^{\mathrm{s}}\zeta_{\mathrm{D}} T; \qquad \gamma_B = (1 + 0.88\alpha^{3/2})\gamma_{\mathrm{D}}, \tag{10}$$

$$\Phi^{\mathrm{s}} = \left(\mu_{\mathrm{b}}^{\mathrm{s}} - \frac{2}{3}\mu_{\mathrm{e}}^{\mathrm{s}}\right)\left(\frac{\partial u^{\mathrm{s}}}{\partial z} + \frac{1}{r}\frac{\partial}{\partial r}(rv^{\mathrm{s}})\right)^2 + 2\mu_{\mathrm{e}}^{\mathrm{s}}\left(\left(\frac{\partial v^{\mathrm{s}}}{\partial r}\right)^2 + \left(\frac{v^{\mathrm{s}}}{r}\right)^2 + \left(\frac{\partial u^{\mathrm{s}}}{\partial z}\right)^2\right) + \mu_{\mathrm{e}}^{\mathrm{s}}\left(\frac{\partial u^{\mathrm{s}}}{\partial r} + \frac{\partial v^{\mathrm{s}}}{\partial z}\right)^2, \tag{11}$$

$$p^{\mathrm{s}} = \alpha\rho^{\mathrm{s}} T(1 + 4\eta g_0 \alpha); \qquad \mu_{\mathrm{b}}^{\mathrm{s}} = \frac{8\rho^{\mathrm{s}} d\eta g_0 \alpha^2}{3}\left(\frac{T}{\pi}\right)^{1/2}, \tag{12}$$

$$\mu_{\mathrm{e}}^{\mathrm{s}} = \frac{\mu^{\mathrm{s}*}}{g_0}\left(1 + \frac{8}{5}\eta g_0\alpha\right)\left(1 + \frac{8}{5}(3\eta - 2)\eta g_0\alpha\right) + \frac{3}{5}\mu_{\mathrm{b}}^{\mathrm{s}}, \tag{13}$$

$$k_T^{\mathrm{s}} = \frac{k^{\mathrm{s}*}}{g_0}\left(1 + \frac{12}{5}\eta g_0\alpha\right)\left(1 + \frac{12}{5}\eta(4\eta - 3)\eta g_0\alpha\right) + \frac{3}{2}\mu_{\mathrm{b}}^{\mathrm{s}}, \tag{14}$$

$$k_\alpha^{\mathrm{s}} = \frac{k^{\mathrm{s}*}}{g_0}\left(1 + \frac{12}{5}\eta g_0\alpha\right)\frac{12}{5}(2\eta - 1)(\eta - 1)\frac{\mathrm{d}}{\mathrm{d}\alpha}(\eta g_0 \alpha^2)\frac{T}{\alpha}, \tag{15}$$

$$\mu^{\mathrm{s}*} = \frac{\mu^{\mathrm{s}'}}{1 + (2\zeta_{\mathrm{D}}\mu^{\mathrm{s}'}/\alpha\rho^{\mathrm{s}} g_0 T)}; \qquad \mu^{\mathrm{s}'} = \frac{5\pi\rho^{\mathrm{s}} d(T/\pi)^{1/2}}{96\eta(2-\eta)}, \tag{16}$$

$$k^{\mathrm{s}*} = \frac{k^{\mathrm{s}'}}{1 + (6\zeta_{\mathrm{D}}k^{\mathrm{s}'}/5\alpha\rho^{\mathrm{s}} g_0 T)}; \qquad k^{\mathrm{s}'} = \frac{75\pi\rho^{\mathrm{s}} d(T/\pi)^{1/2}}{48\eta(41 - 33\eta)}, \tag{17}$$

$$\eta = \frac{1+e}{2}; \qquad C_{\mathrm{D}} Re^{\mathrm{s}} = 24 + \frac{18}{5}(Re^{\mathrm{s}})^{0.687}; \qquad g_0 = \left(1 - \frac{\alpha}{\alpha_{\mathrm{MX}}}\right)^{-2.5\alpha_{\mathrm{MX}}}. \tag{18}$$

In these equations, γ_{c} and γ_{D} are the collisional and drag dissipation terms, respectively; γ_B is a term that describes energy transfer between the fluctuating and the mean flows; Φ^{s} is a viscous dissipation term that appears as a volumetric source in the granular-temperature equation; Re^{s} is the particle Reynolds number:

$$\frac{\rho^{\mathrm{f}} d\sqrt{(u_i^{\mathrm{f}})^2 - 2u_i^{\mathrm{f}}u_i^{\mathrm{s}} + (u_i^{\mathrm{s}})^2}}{\mu^{\mathrm{f}}};$$

g_0 is an equilibrium radial distribution function [38]; e is the particle coefficient of restitution; and α_{MX} is the solid-phase concentration at maximum packing.

2.2.2. Fluid phase.

$$\mu_{\mathrm{e}}^{\mathrm{f}} = \mu_{\mathrm{a}}^{\mathrm{f}} + \mu_F^{\mathrm{f}}; \qquad \mu_{\mathrm{a}}^{\mathrm{f}} = \mu^{\mathrm{f}}\mu_{\mathrm{r}}^{\mathrm{f}}(\alpha), \tag{19}$$

$$\mu_F^{\mathrm{f}} = \rho^{\mathrm{f}}(C_{\mathrm{s}}\Delta)^2 S; \qquad \mu_{\mathrm{b}}^{\mathrm{f}} = 0, \tag{20}$$

$$S = \left\{ 2\left[\left(\frac{\partial u^{\mathrm{f}}}{\partial z} \right)^2 + \left(\frac{\partial v^{\mathrm{f}}}{\partial r} \right)^2 + \left(\frac{v^{\mathrm{f}}}{r} \right)^2 \right] + \left[\frac{\partial u^{\mathrm{f}}}{\partial r} + \frac{\partial v^{\mathrm{f}}}{\partial z} \right]^2 - \frac{2}{3}\left[\frac{\partial u^{\mathrm{f}}}{\partial z} + \frac{1}{r}\frac{\partial}{\partial r}(r v^{\mathrm{f}}) \right]^2 \right\}^{1/2}, \tag{21}$$

$$\mu_{\mathrm{r}}^{\mathrm{f}}(\alpha) = (1 - \alpha - 0.33\alpha^2)^{-5/2}. \tag{22}$$

In the volume-average description of the fluid phase, terms appear that are analogous to the subgrid-scale Reynolds stress tensor encountered in large eddy simulations (LES) of turbulent flows [50].The μ_F^{f} term and its expression are related to the approximation of this subgrid-scale stress tensor using a model akin to the Smagorinsky model [50,51] developed in the context of LES: C_{s} lies between 0.1 (for coarse grid) and 0.2 (for fine grid); Δ is a linear measure of the grid size.

3. NUMERICAL METHOD

The proposed numerical method is a CVFEM based on a primitive-variables, co-located, equal-order formulation: it works directly with the velocity components, pressure and granular temperature; these dependent variables are stored at the same nodes in the finite element mesh and are interpolated over the same elements. This CVFEM is constructed by adapting and extending ideas from earlier CVFEMs for single-phase incompressible fluid flows proposed by Baliga and Patankar [52], Prakash and Patankar [53], Schneider and Raw [54,55], Masson *et al*. [56], and Saabas and Baliga [57].

A detailed description of a CVFEM for the simulation of dilute-concentration gas–solid particle flows has been published recently [48]. This CVFEM [48] is closely related to the numerical method used in this paper. Furthermore, details of the CVFEM for single-phase flows are available in Reference [56]. Therefore, for sake of conciseness, only a very brief description of the method, with appropriate emphasis on the aspects relevant to the successful simulation of *dense* gas–solid particle flows, will be presented in this section.

3.1. Domain discretization

A longitudinal cross-section of the axisymmetric domain of interest is first divided into three-node triangular elements. Then the centroids of the elements are joined to the midpoints of the corresponding sides. This creates polygonal control volumes around each node in the finite element mesh. The longitudinal cross-section of a sample domain discretization is shown in Figure 1: the solid lines denote the domain and element boundaries; the dashed lines represent the control-volume faces; and the shaded areas show the control volumes associated with one internal node and one boundary node.

The discretization of the longitudinal cross-section is rotated through 2π radians about the axis of symmetry. The result is a discretization of the axisymmetric calculation domain into torus elements of triangular cross-section, and torus control volumes of polygonal cross-section. In the rest of the paper, the torus elements and torus control volumes will be referred to simply as triangular (three-node) elements and polygonal control volumes, respectively.

3.2. Integral conservation equation

Consider a typical node i in the calculation domain: it could be an internal node, such as the one shown in Figure 2(a), or a boundary node, similar to the one shown in Figure 2(b). An integral formulation corresponding to Equation (1) can be obtained by applying the appropriate conservation principle for the dependent variable ϕ to a suitably chosen control volume.

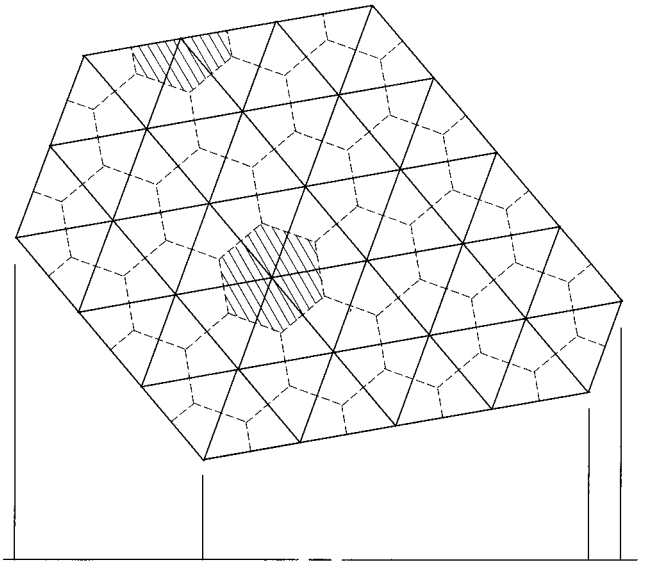

Figure 1. Discretization of the longitudinal cross-section of a calculation domain.

The resulting integral conservation equation, when applied to the polygonal control volume surrounding node i in Figure 2, can be written as

$$\left[\int_a^o \vec{J}\cdot\vec{n}2\pi r\,\mathrm{d}s+\int_o^c \vec{J}\cdot\vec{n}2\pi r\,\mathrm{d}s-\int_{iaoc} S_\phi\,\mathrm{d}\mathscr{V}+\int_{iaoc}\frac{\partial}{\partial t}(\beta\rho\phi)\,\mathrm{d}\mathscr{V}\right]$$
$$+[\text{similar contributions from other elements surrounding node } i]$$
$$+[\text{boundary contributions, if applicable}]=0, \tag{23}$$

where $\vec{n}$ is a unit vector normal to the differential length element, ds, and pointing outward with respect to the control volume. $\vec{J}$ is the combined convection–diffusion flux of ϕ:

$$\vec{J}=\vec{J}_D+\beta\vec{J}_C, \tag{24}$$

$$\vec{J}_D=-\Gamma_e\nabla\phi, \tag{25}$$

$$\vec{J}_C=\rho\vec{V}^m\phi. \tag{26}$$

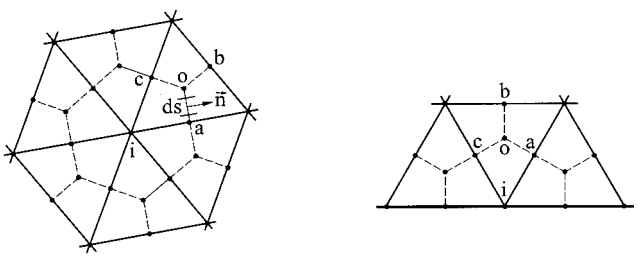

Figure 2. Typical control volumes surrounding (a) an internal node; and (b) a boundary node.

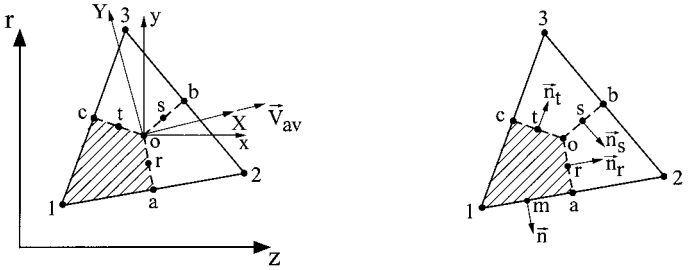

Figure 3. Typical triangular element: (a) global and local co-ordinate systems; (b) unit normals.

With reference to Equation (26), the superscript m is attached to the velocity vector in order to emphasize its connection to the mass flux: this velocity is interpolated in a special way, as is discussed in the next section. The form of Equation (23) emphasizes that it can be assembled by using an element-by-element procedure.

3.3. Interpolation functions

The derivation of algebraic approximations to the integral conservation equations requires the specification of element-based interpolation functions for the dependent variable ϕ, the velocity components u and v, diffusion coefficients Γ_e and Γ_b, source term S_ϕ, mass density ρ, and volume concentration β. As was stated earlier, specific forms of ϕ, u, v, Γ_e, Γ_b, ρ and β are given in Table I.

The interpolation functions are specific to each element. For convenience in the formulation of these functions and subsequent derivations, a local (x, y) co-ordinate system is defined in each element, such that the origin is at the centroid of the triangular element, the x-axis is in the direction of z, and the y-axis is in the direction of r, as shown in Figure 3(a).

3.3.1. Diffusion coefficients, density and sources. The diffusion coefficients Γ_e and Γ_b are stored at the vertices of the triangular elements. $\bar{\Gamma}_e$ and $\bar{\Gamma}_b$ are assumed to prevail over the corresponding element. $\bar{\Gamma}_e$ and $\bar{\Gamma}_b$ are computed by assuming a linear variation of Γ_e and Γ_b, respectively:

$$\bar{\Gamma}_e = \frac{1}{3}(\Gamma_{e1} + \Gamma_{e2} + \Gamma_{e3}), \tag{27}$$

$$\bar{\Gamma}_b = \frac{1}{3}(\Gamma_{b1} + \Gamma_{b2} + \Gamma_{b3}), \tag{28}$$

where Γ_{e1}, Γ_{e2} and Γ_{e3} are the values of Γ_e stored at the vertices 1, 2 and 3, defined in Figure 3. Similar notation is used for Γ_b. This treatment is convenient in this formulation because most of the diffusion coefficients, namely μ_a^f, μ_b^f, μ_e^s, μ_b^s, k_T^s and k_α^s, are functions of the dependent variables only and not of their derivatives. In cases where the diffusion coefficient is expressed as a function of space derivatives of the dependent variables, such as for μ_F^f, volume-average space derivatives associated with each control volume are used first to evaluate the corresponding nodal values. The element contribution of S_{cyl} is evaluated assuming that the values at the vertices prevail over the corresponding portions of the control volumes within that element.

In each triangular element, the centroidal value of ρ is assumed to prevail over the corresponding element. It should be noted, however, that in this particular work, the density of the solid and fluid materials, ρ^s and ρ^f, respectively, are assumed to remain constant throughout the calculation domain.

The source term S_ϕ is linearized, if needed, and expressed in the form [45]:

$$S_\phi = S_C + S_P\phi. \tag{29}$$

In each triangular element, the values of S_C and S_P are stored at the vertices, and are assumed to prevail over the corresponding portions of the control volumes within that element. Thus within *each element*, three sets of S_C and S_P are stored: S_{C1}, S_{C2}, S_{C3}, S_{P1}, S_{P2} and S_{P3}.

3.3.2. Mass flow rates. In the calculation of mass flow rates across the control-volume faces, the velocity is denoted by

$$\vec{V}^m = u^m\vec{i} + v^m\vec{j}. \tag{30}$$

When mass flow rates of the solid phase are considered, $u^m = u^s$ and $v^m = v^s$, and u^m and v^m are interpolated linearly in each element. However, when the mass flow rates of the fluid phase are considered, a special treatment, borrowed from the works of Prakash and Patankar [53], Masson *et al*. [56], and Saabas and Baliga [57] is used to prevent the occurrence of spurious pressure oscillations in the proposed co-located equal-order CVFEM. The development of this special interpolation is based on the discretized fluid-phase momentum conservation equations. Therefore, it will be presented later in this section.

3.3.3. ϕ in diffusion terms. In the derivation of algebraic approximations to surface integrals of diffusion fluxes (Equations (23) and (25)), the dependent variable ϕ is interpolated linearly in each element:

$$\phi = Ax + By + C. \tag{31}$$

An equivalent, and perhaps more elegant, development of this linear interpolation on triangular elements could be performed using barycentric or area co-ordinates, traditionally employed in FEMs [58]. In order to be consistent with the derivations in the following sections, however, the above-stated development is preferred in this case. It should also be noted that with such linear interpolation functions, Delaunay triangulation is required to ensure that algebraic approximations of the diffusion transport terms contribute positively to the coefficients in the discretized equations. Barth [59] has presented a formal proof of this statement for two-dimensional planar problems: this proof applies when the diffusion coefficient is a constant.

3.3.4. ϕ in convection terms. In the derivation of algebraic approximations to surface integrals of the convective fluxes (Equations (23) and (26)), a mass-weighted skew upwind scheme (MAW), originally introduced by Schneider and Raw [54], is used.

The MAW scheme defines a mass-weighted average of ϕ at each of the three control surfaces of a triangular element (Figure 3(b)), namely ϕ_r, ϕ_s, ϕ_t, in the following manner: let

$$\dot{m}_r = \int_o^a \beta\rho\,\vec{V}^m \cdot \vec{n}_r 2\pi r \,\mathrm{d}s; \qquad \dot{m}_s = \int_o^b \beta\rho\,\vec{V}^m \cdot \vec{n}_s 2\pi r \,\mathrm{d}s; \qquad \dot{m}_t = \int_o^c \beta\rho\,\vec{V}^m \cdot \vec{n}_t 2\pi r \,\mathrm{d}s, \tag{32}$$

where $\vec{n}_r$, $\vec{n}_s$ and $\vec{n}_t$ are unit normals, as shown in Figure 3(b).

$$\phi_r = \begin{cases} f^+\phi_t + (1-f^+)\phi_1 & \text{where } f^+ = \min\left[\max\left(-\dfrac{\dot{m}_t}{\dot{m}_r}, 0\right), 1\right] \text{ if } \dot{m}_r > 0 \\ f^-\phi_s + (1-f^-)\phi_2 & \text{where } f^- = \min\left[\max\left(-\dfrac{\dot{m}_s}{\dot{m}_r}, 0\right), 1\right] \text{ if } \dot{m}_r < 0 \end{cases}, \tag{33}$$

$$\phi_s = \begin{cases} f^+\phi_t + (1-f^+)\phi_3 & \text{where } f^+ = \min\left[\max\left(\dfrac{\dot{m}_t}{\dot{m}_s}, 0\right), 1\right] \text{ if } \dot{m}_s > 0 \\ f^-\phi_r + (1-f^-)\phi_2 & \text{where } f^- = \min\left[\max\left(-\dfrac{\dot{m}_r}{\dot{m}_s}, 0\right), 1\right] \text{ if } \dot{m}_s < 0 \end{cases}, \tag{34}$$

$$\phi_t = \begin{cases} f^+\phi_r + (1-f^+)\phi_1 & \text{where } f^+ = \min\left[\max\left(-\dfrac{\dot{m}_r}{\dot{m}_t}, 0\right), 1\right] \text{ if } \dot{m}_t > 0 \\ f^-\phi_s + (1-f^-)\phi_3 & \text{where } f^- = \min\left[\max\left(\dfrac{\dot{m}_s}{\dot{m}_t}, 0\right), 1\right] \text{ if } \dot{m}_t < 0 \end{cases}. \tag{35}$$

These mass-weighted averages of ϕ are assumed to prevail over each control surface when the surface integrals of the convective fluxes (Equations (23) and (26)) are evaluated. It should be noted that in this scheme, to obtain expressions for ϕ_r, ϕ_s and ϕ_t in terms of ϕ_1, ϕ_2 and ϕ_3, a 3×3 matrix of element-interpolation coefficients must be inverted. Further details are available in the work of Masson [49].

3.3.5. Fluid-phase pressure p^f and solid-phase pressure p^s. Fluid-phase and solid-phase pressures are interpolated linearly in each element. With respect to the local (x, y) co-ordinate system shown in Figure 3(a):

$$p^{\mathrm{f}} = d^{\mathrm{f}}x + e^{\mathrm{f}}y + f^{\mathrm{f}}, \tag{36}$$

$$p^{\mathrm{s}} = d^{\mathrm{s}}x + e^{\mathrm{s}}y + f^{\mathrm{s}}. \tag{37}$$

It should be noted that p^{s} is a function of the dependent variables T and α, as given in Equation (12). The interpolation function given in Equation (37) is used to obtain convenient and adequate approximations of the gradients of p^{s} that appear in the solid-phase momentum equations.

3.3.6. Volume concentrations. In most of the available finite volume methods for two-phase flows, the function used to interpolate α is based on the upwind scheme [32–36]. In this work, an adaptation of the MAW scheme described previously has been implemented.

The modified MAW scheme defines a material mass-weighted average of α at integration points on each of the three control surfaces of a triangular element (Figure 3(b)), namely α_r, α_s, α_t, in a similar manner to that for the mass-weighted average of ϕ. Equations (33)–(35) are used with the following modifications: replace ϕ_r, ϕ_s and ϕ_t with α_r, α_s and α_t, respectively; replace ϕ_1, ϕ_2 and ϕ_3 with α_1, α_2 and α_3, respectively; and $\dot{m}_r$, $\dot{m}_s$ and $\dot{m}_t$ with $\dot{M}_r^{\mathrm{s}}$, $\dot{M}_s^{\mathrm{s}}$ and $\dot{M}_t^{\mathrm{s}}$, respectively, where

$$\dot{M}_r^{\mathrm{s}} = \int_o^a \rho^{\mathrm{s}}\vec{V}^{\mathrm{s}} \cdot \vec{n}_r 2\pi r \, \mathrm{d}s; \qquad \dot{M}_s^{\mathrm{s}} = \int_o^b \rho^{\mathrm{s}}\vec{V}^{\mathrm{s}} \cdot \vec{n}_s 2\pi r \, \mathrm{d}s; \qquad \dot{M}_t^{\mathrm{s}} = \int_o^c \rho^{\mathrm{s}}\vec{V}^{s} \cdot \vec{n}_t 2\pi r \, \mathrm{d}s. \tag{38}$$

ϵ is calculated using $\epsilon + \alpha = 1$. These solid-material mass-weighted averages of α and ϵ are assumed to prevail over each control surface when the mass flow rates in the integral continuity and momentum equations are evaluated.

3.4. Discretization equations

The discretization equations are obtained by first deriving algebraic approximations to the element contributions and the boundary contributions, if applicable, and then assembling these contributions appropriately. The algebraic approximations of the element and boundary contributions are obtained by performing the surface and volume integrals of Equation (23) analytically whenever possible, otherwise numerically.

3.4.1. Discretized u^f and v^f equations. The discretized momentum equations are derived and assembled using element-by-element procedures. The resulting u^{f} and v^{f} discretization equations for the fluid phase at a node i can be cast in the forms

$$\left(ac_i^{u\mathrm{f}} + K_i \mathscr{V}_{\mathrm{cv}} + \frac{\epsilon_i \rho^{\mathrm{f}} \mathscr{V}_{\mathrm{cv}}}{\Delta t}\right) u_i^{\mathrm{f}} = \sum_{nb} ac_{nb}^{u\mathrm{f}} u_{nb}^{\mathrm{f}} + b^{u\mathrm{f}} + K_i u_i^{\mathrm{s}} \mathscr{V}_{\mathrm{cv}} + \frac{\epsilon_i^* \rho^{\mathrm{f}} \mathscr{V}_{\mathrm{cv}}}{\Delta t} u_i^{\mathrm{f}*} + \epsilon_i \mathscr{V}_{\mathrm{cv}} \left(-\overline{\frac{\partial p^{\mathrm{f}}}{\partial z}}\right), \tag{39}$$

$$\left(ac_i^{v\mathrm{f}} + K_i \mathscr{V}_{\mathrm{cv}} + \frac{\epsilon_i \rho^{\mathrm{f}} \mathscr{V}_{\mathrm{cv}}}{\Delta t}\right) v_i^{\mathrm{f}} = \sum_{nb} ac_{nb}^{v\mathrm{f}} v_{nb}^{\mathrm{f}} + b^{v\mathrm{f}} + K_i v_i^{\mathrm{s}} \mathscr{V}_{\mathrm{cv}} + \frac{\epsilon_i^* \rho^{\mathrm{f}} \mathscr{V}_{\mathrm{cv}}}{\Delta t} v_i^{\mathrm{f}*} + \epsilon_i \mathscr{V}_{\mathrm{cv}} \left(-\overline{\frac{\partial p^{\mathrm{f}}}{\partial r}}\right). \tag{40}$$

The bar over the pressure gradient denotes volume average associated with the control volume $\mathscr{V}_{\mathrm{cv}}$. The superscript * means that the corresponding dependent variable is evaluated at the previous time step.

3.4.2. Discretized u^s and v^s equations. Using similar element-by-element procedures, the resulting u^{s} and v^{s} discretization equations for the solid phase at a node i can be obtained and cast in the forms

$$\begin{aligned}&\left(ac_i^{u\mathrm{s}} + K_i \mathscr{V}_{\mathrm{cv}} + \frac{\alpha_i \rho^{\mathrm{s}} \mathscr{V}_{\mathrm{cv}}}{\Delta t}\right) u_i^{\mathrm{s}} \\ &= \sum_{nb} ac_{nb}^{u\mathrm{s}} u_{nb}^{\mathrm{s}} + b^{u\mathrm{s}} + \mathscr{V}_{\mathrm{cv}} \left(-\overline{\frac{\partial p^{\mathrm{s}}}{\partial z}}\right) + K_i u_i^{\mathrm{f}} \mathscr{V}_{\mathrm{cv}} + \frac{\alpha_i^* \rho^{\mathrm{s}} \mathscr{V}_{\mathrm{cv}}}{\Delta t} u_i^{\mathrm{s}*} + \alpha_i \mathscr{V}_{\mathrm{cv}} \left(-\overline{\frac{\partial p^{\mathrm{f}}}{\partial z}}\right),\end{aligned} \tag{41}$$

$$\begin{aligned}&\left(ac_i^{v\mathrm{s}} + K_i \mathscr{V}_{\mathrm{cv}} + \frac{\alpha_i \rho^{\mathrm{s}} \mathscr{V}_{\mathrm{cv}}}{\Delta t}\right) v_i^{\mathrm{s}} \\ &= \sum_{nb} ac_{nb}^{v\mathrm{s}} v_{nb}^{\mathrm{s}} + b^{v\mathrm{s}} + \mathscr{V}_{\mathrm{cv}} \left(-\overline{\frac{\partial p^{\mathrm{s}}}{\partial r}}\right) + K_i v_i^{\mathrm{f}} \mathscr{V}_{\mathrm{cv}} + \frac{\alpha_i^* \rho^{\mathrm{s}} \mathscr{V}_{\mathrm{cv}}}{\Delta t} v_i^{\mathrm{s}*} + \alpha_i \mathscr{V}_{\mathrm{cv}} \left(-\overline{\frac{\partial p^{\mathrm{f}}}{\partial r}}\right).\end{aligned} \tag{42}$$

The contribution of the momentum interaction term is stated explicitly in these equations in order to clearly represent the coupling between the momentum equations of the two phases. This coupling will be used in the solution procedure presented later. Further manipulations of the unsteady contributions are needed in the calculation of mass flow rates (see Equations (45)–(46)); therefore, they are also stated explicitly in the previous equations. The solid-phase pressure gradient terms that appear in Equations (41) and (42) are presented as separate terms in the discretized equations for the sake of clarity, however, in the actual implementation, they could be included in $b^{u\mathrm{s}}$ and $b^{v\mathrm{s}}$.

3.4.3. Discretized T equation. The solid-phase fluctuating kinetic energy is always positive. To ensure a positive granular temperature, special attention is needed in the linearization of the source terms. Patankar [45] has suggested the use of positive S_C and negative S_P to ensure that the always-positive dependent variables are indeed positive during the solution process. In order to satisfy Patankar's recommendations, the following strategy is adopted in this work: (i) contributions from the collisional and drag dissipation source terms are divided and multiplied by T, and γ_c/T^* and γ_D/T^* are included in S_P; (ii) the energy transfer term γ_B, and the viscous dissipation Φ^s, are included in S_C; and (iii) similarly, the solid-phase pressure work W_p, and the diffusion induced by concentration gradients S_α (which could be either positive or negative) are appropriately included either in S_C or S_P, depending on the sign of their respective element contribution. Procedures for the discretization of the unsteady terms and the convection and diffusion transport terms are similar to those described earlier. The resulting T discretization equation at a node i can be cast in the general form

$$ac_i^T T_i = \sum_{nb} ac_{nb}^T T_{nb} + b^T. \tag{43}$$

3.4.4. Discretized equations for p^f and α

3.4.4.1. Discretized p^f equation. In each element, the velocity $\vec{V}^m$ can be expressed in terms of its components in the z- and r-directions, u^m and v^m, respectively, as shown in Equation (30). Interpolation functions for u^m and v^m must first be prescribed in order to approximate the fluid-phase mass flux integrals. First, the fluid-phase discretized momentum equations (39) and (40) are rewritten in the following manner:

$$u_i^f = \hat{u}_i^f + d_i^{uf}\left(-\overline{\frac{\partial p^f}{\partial z}}\right), \qquad v_i^f = \hat{v}_i^f + d_i^{vf}\left(-\overline{\frac{\partial p^f}{\partial r}}\right), \tag{44}$$

where

$$\hat{u}_i^f = \frac{\sum_{nb} ac_{nb}^{uf} u_{nb}^f + b^{uf} + K_i u_i^s \mathscr{V}_{cv} + (\rho^f \mathscr{V}_{cv}/\Delta t)(\epsilon_i^* u_i^{f*} - \epsilon_i u_i^f)}{ac_i^{uf} + K_i \mathscr{V}_{cv}}, \qquad d_i^{uf} = \frac{\epsilon_i \mathscr{V}_{cv}}{ac_i^{uf} + K_i \mathscr{V}_{cv}}, \tag{45}$$

$$\hat{v}_i^f = \frac{\sum_{nb} ac_{nb}^{vf} v_{nb}^f + b^{vf} + K_i v_i^s \mathscr{V}_{cv} + (\rho^f \mathscr{V}_{cv}/\Delta t)(\epsilon_i^* v_i^{f*} - \epsilon_i v_i^f)}{ac_i^{vf} + K_i \mathscr{V}_{cv}}, \qquad d_i^{vf} = \frac{\epsilon_i \mathscr{V}_{cv}}{ac_i^{vf} + K_i \mathscr{V}_{cv}}. \tag{46}$$

For the evaluation of the fluid-phase mass fluxes on the faces a–o and o–c (Figure 3), the fluid-phase velocity components are written as

$$u^m = \hat{u}^f + d^{uf}\left(-\frac{\partial p^f}{\partial z}\right)_{ele}, \qquad v^m = \hat{v}^f + d^{vf}\left(-\frac{\partial p^f}{\partial r}\right)_{ele}, \tag{47}$$

where the pseudo-velocity components and the pressure-gradient coefficients, $\hat{u}^f$, $\hat{v}^f$, d^{uf} and d^{vf}, are interpolated linearly from the corresponding values at the vertices of the element, and $(-\partial p^f/\partial z)_{ele}$ and $(-\partial p^f/\partial r)_{ele}$ are the pressure gradients in the element being considered. This procedure prevents pressure checkerboarding in FVMs [45] and in co-located CVFEMs [56,60] for incompressible flows. Similar interpolation of the velocity components in the mass-flux terms have been successfully used by Peric *et al.* [61], Rice and Schnipke [62], and Rhie and Chow [63].

In the derivation of algebraic approximations to integrals of fluid-phase mass flow rates, u^m and v^m are interpolated in each element by the functions given in Equation (47). The same functions are also used to approximate integrals that represent the mass flow rates in the fluid-phase momentum equations. Using these interpolation functions, the contributions of element 123 (Figure 3) to the fluid-phase mass conservation equation for the node 1 can be calculated. Similarly, in general, addition of the contributions of the elements surrounding the node i yields the complete discretized fluid-phase mass conservation equation.

When explicit algebraic expressions for the pressure gradient terms are substituted into the interpolation functions for the mass-flux velocity components (Equation (47)), and then these interpolation functions are used in the element contributions to the discretized fluid-phase mass conservation equations, discretized equations for p^{f} are obtained.

A compact representation of the discretized p^{f} equation for a typical node i is

$$ac_i^p p_i^{\mathrm{f}} = \sum_{nb} ac_{nb}^p p_{nb}^{\mathrm{f}} + b^p. \tag{48}$$

3.4.4.2. Discretized α equation. For the evaluation of the solid-phase mass fluxes on the faces $a-o$ and $o-c$ (Figure 3), the mass-flux velocity components are written as

$$u^m = u^{\mathrm{s}}, \qquad v^m = v^{\mathrm{s}}, \tag{49}$$

and u^{s}, v^{s} are interpolated linearly from the corresponding values at the vertices of the element.

Addition of the contributions of the elements surrounding the point i yields the complete discretized solid-phase mass conservation equation. These discretized equations are used to compute the solid-phase concentration, α; ϵ is computed using $\alpha + \epsilon = 1$.

A compact representation of the discretized α equation for a typical node i is

$$ac_i^\alpha \alpha_i = \sum_{nb} ac_{nb}^\alpha \alpha_{nb} + b^\alpha. \tag{50}$$

3.4.4.3. Discussion. Carver [34] suggests subtraction of the fluid-phase continuity equation from the solid-phase continuity equation to derive a discretization equation for α, and an addition of these equations in the derivation of the discretization equation for p^{f}, so as to explicitly account for the coupling between the phases in the calculation of α and p^{f}. This treatment is only appropriate when local mass conservation is ensured over each control-volume for each phase individually, as in the FVM used by Carver [34]. In the proposed co-located equal-order CVFEM, for problems that involve inflows and outflows, α is prescribed at all nodes located on the inflow boundaries, and p^{f} is prescribed at one (or more) node(s) located at the outflow boundaries: thus, for the control volumes surrounding the nodes on the inflow boundaries, local mass conservation of the solid phase is not explicitly imposed; and local mass conservation of the fluid phase is not explicitly imposed for the control volumes associated with the nodes on the outflow boundaries at which p^{f} is prescribed. Thus, at nodes on the inflow and outflow boundaries, the treatment proposed by Carver [34] could not be incorporated into the proposed CVFEM. Furthermore, the construction of a fluid-phase pressure equation based on the sum of the fluid- and solid-phase continuity equations can be realized only when the solid-phase mass-flow related velocities are calculated using a treatment similar to the fluid-phase mass-flow related velocities. The use of such solid-phase mass-flow related velocities has been implemented for the solution of dilute gas–solid particle flows [46–48], but this approach leads to severe convergence problems at high solid-phase concentrations. Therefore, in this work, the discretization equations for α are obtained from the continuity equation for the solid phase, and the solid-phase mass-flow related velocities at the integration points are

obtained from linear interpolation of the solid-phase nodal velocities; and only the fluid-phase continuity equation is used to derive the discretization equations for p^f. In each iteration, therefore, the coupling between the two phases is not *directly* accounted for in the calculation of α and p^f, but this did not lead to any major difficulties. It should be also noted that in *dilute* gas–solid particle flows, the proposed discretization equations for α do not need any special treatment to ensure physically realistic solutions [46–48], while the linear combination approach suggested by Carver [34] does: the discretized source term of the proposed discretized concentration equation is always equal to or greater than zero, as are all the coefficients in this equation. This feature ensures that $\alpha \geq 0$. In addition, since $\alpha \ll 1$ in *dilute* gas–solid particle flows, there is no need to incorporate any special procedures to ensure that $\alpha < 1$ during the iterative solution procedure. However, for problems involving higher solid-phase concentrations, an appropriately small time step was needed to ensure that $\alpha < \alpha_{MX}$ throughout the solution procedure, as will be discussed later in Section 4.

3.5. Overall solution algorithm

The discretization equations form two sets of coupled non-linear algebraic equations. In this work, *at each time step*, a modified version of the iterative variable adjustment procedure proposed by Saabas and Baliga [57] for single-phase flow, and recently applied to dilute gas–solid particle flows by Masson and Baliga [46–48], was used to solve the mathematical model:

1. Start with guessed or available velocities, fluid-phase pressure, solid-phase concentration, and granular-temperature fields.
2. Calculate the fluid- and solid-phase diffusion coefficients, and the solid-phase pressure, using the constitutive equations.
3. Calculate coefficients in the discretized unsteady momentum equations *without* including contributions of the fluid-phase pressure-gradient terms.
4. Calculate the fluid-phase pseudo-velocities and pressure-gradient coefficients.
5. Calculate coefficients in the discretized fluid-phase pressure equations, and solve these equations to obtain updated values of p^f.
6. Add contributions of the fluid-phase pressure-gradient terms to the appropriate coefficients of the discretized z-momentum equations calculated in Step 3, and solve for u^f and u^s, *simultaneously*.
7. Add contributions of the fluid-phase pressure-gradient terms to the appropriate coefficients of the discretized r-momentum equations calculated in Step 3, and solve for v^f and v^s, *simultaneously*.
8. Calculate coefficients of the discretized equations for α, and solve these equations to obtain updated values of α.
9. Calculate ϵ $(= 1 - \alpha)$.
10. Calculate coefficients in the discretized granular-temperature equations, and solve these equations to obtain updated values of T.
11. Return to Step 2, and repeat until appropriate convergence criteria are satisfied.

A fully-implicit unsteady formulation [45] is used in this work. It should be noted here that in the proposed method, the solution of steady-state problems is also obtained through the use of a fully implicit unsteady formulation. This approach is related to the solution of the coupled, non-linear, *steady-state* equations using iterative methods with underrelaxation [45]. In the two-fluid model considered in this work, there are two sets of governing equations, one

related to the fluid phase and one to the solid phase. In the iterative solution of the steady state equations, it is often necessary to prescribe different relaxation factors for each of the two sets of discretization equations, in order to ensure convergence of the overall algorithm. In the unsteady formulation, however, only the time step must be given. This time step will naturally ensure a common evolution of the solution for each set of equations, and this results in a robust numerical solution algorithm. In the choice of a suitable time step, guidance is obtained from physical quantities such as the value of the particle relaxation time, which can be estimated using the expression $\tau^{s}_{rel} = \frac{4}{3}(\rho^{s} d^2/\mu^{f} C_D Re^{s})$. Values of the time step (Δt) less than τ^{s}_{rel} were used in this work.

In this work, the solution was considered to be converged when the non-dimensional average, absolute, residue for each set of discretized equations was $< 10^{-10}$. If the unsteady formulation is used only to facilitate the solution of steady-state problems, then it is not necessary to obtain iterative convergence (Step 11) in this procedure at each time step. Instead, Steps 2–10 are executed in sequence only once per time step, and the solution is marched in time until steady-state conditions prevail.

In order to facilitate implementation and testing of the proposed CVFEM, structured grids were used in this work: the nodes in the finite element mesh lie along non-orthogonal lines that allow (I, J) indexing. Thus, in steps 5, 8 and 10, a line Gauss–Seidel algorithm based on the tri-diagonal matrix algorithm [45] was used to solve the discretized equations for p^{f}, α and T, respectively. In steps 6 and 7, a line Gauss–Seidel method based on a coupled-equation line solver [45] was used.

The momentum coupling source terms allow a direct accounting of the coupling between the solid- and fluid-phase momentum equations in the above-mentioned solution algorithm. The simultaneous solution of the solid- and fluid-phase momentum equations in Steps 6 and 7 is an important contributor to the robustness of the proposed algorithm. The unsteady formulation also contributes significantly to the robustness of the overall solution procedure by ensuring a similar evolution of the solutions of the fluid- and solid-phase sets of equations.

The modified MAW scheme that is used to interpolate the solid-phase concentration ensures positive coefficients in the discretized solid-phase concentration equation. Furthermore, the solid-phase concentration equation is based on the solid-phase continuity equation only: this yields homogeneous discretized equations everywhere in the domain of interest except at points where the concentration is known. This results in a system of equations that admit only positive values of α, which is a physical requirement of the volume concentration. At high solid-phase concentrations, the discretized solid-phase concentration equations can, in principle, admit values larger than the maximum packing limit, α_{MX}. However, when the concentration is large, the solid-phase pressure appearing in the momentum equation tends to disperse the solid particles and, therefore, reduce the solid-phase volume concentration to values below α_{MX}. However, in the context of the above-mentioned iterative solution algorithm, the effects of the solid-phase pressure are not always large enough to prevent α from reaching values equal to or larger than α_{MX}. In such situations, the use of a smaller time step has been found to be useful in alleviating this difficulty.

The mathematical model given in Section 2 is applicable to values of the solid-phase volume concentration in the range $0 \leq \alpha < \alpha_{MX}$. The overall numerical solution algorithm, however, is *not* capable of handling regions where α is strictly equal to zero: in this work, such regions are assumed to correspond to very small, but non-zero, values of α ($\geq 10^{-10}$).

4. RESULTS AND DISCUSSION

The capabilities of the general granular-temperature model, presented in Section 2, are demonstrated in this section. Simulations of gas–solid particle flows in a vertical pipe and an annular shear cell apparatus are used as test problems, and the results are compared with those of independent numerical and experimental investigations. In another test problem, a dilute-concentration gas–solid particle flow in a duct with a sudden contraction is simulated using the general granular-temperature model, and the results are compared with the solution of a dilute-concentration model [48], in order to assess the capabilities of the general granular-temperature model in the dilute concentration regime. Finally, an idealized laminar split-flow inertial separator is analyzed using the granular-temperature model, allowing a demonstration of the effects of particle–particle collisions on such a flow.

4.1. Vertical pipe flow

Solutions of gas–solid particle flows in a vertical pipe have been obtained by Sinclair and Jackson [39]. Their mathematical model is quite similar to the one used in this paper. It is based on the kinetic theory of gases, and the granular temperature is a dependent variable that appears in their constitutive equations. However, they have only solved these equations in the fully-developed regime, in which the problem becomes one-dimensional (radial). In the fully-developed regime, Sinclair and Jackson [39] have studied a large variety of flows using a numerical method based on an orthogonal collocation scheme.

In this section, gas–solid particle flows in a vertical pipe (see Figure 4) are investigated using the proposed CVFEM, and the results are compared with the numerical results obtained by Sinclair and Jackson [39]. As was stated before, the fully-developed problem is one-dimensional. Here, however, this problem was solved using a two-dimensional formulation. This is obviously not the most efficient formulation for this problem, but it allows a convenient check on the two-dimensional capabilities of the proposed CVFEM. The problem is, therefore, formulated over a pipe of finite length. Periodic boundary conditions were imposed at the ends of the pipe; this approach will be referred to as the 'periodic' formulation.

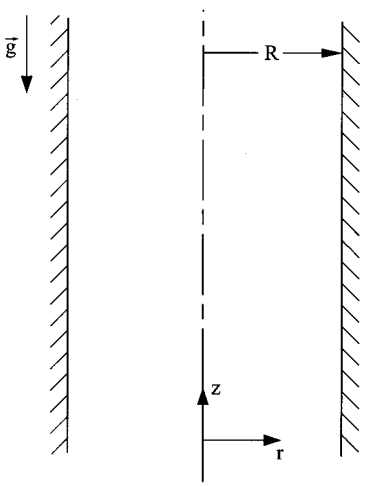

Figure 4. Vertical pipe.

The various physical properties used in the problem solved by Sinclair and Jackson [39], which corresponds to a flow of mineral particles in air at 427°C, are

$$\mu^{\mathrm{f}} = 3.65 \times 10^{-5} \text{ Pa} \cdot \text{s}, \qquad \rho^{\mathrm{f}} = 4.4 \times 10^{-1} \text{ kg m}^{-3}, \tag{51}$$

$$\rho^{\mathrm{s}} = 2.5 \times 10^{3} \text{ kg m}^{-3}, \qquad \alpha_{\mathrm{MX}} = 0.65, \qquad v_{\mathrm{t}} = 1.29 \text{ m s}^{-1}, \tag{52}$$

$$d = 1.5 \times 10^{-4} \text{ m}, \qquad R = 1.5 \times 10^{-2} \text{ m}, \tag{53}$$

v_{t} is the terminal velocity of fall of a single particle under gravity; R is the radius of the pipe; and α_{MX} is the solid-phase concentration at maximum packing.

With reference to the general mathematical model introduced in Section 2, some modifications and adaptations were required in order to obtain solutions which correspond to the results of Sinclair and Jackson [39]. In particular, the following relations for the relative viscosity, the drag coefficient, and g_0 were used:

$$\mu_{\mathrm{r}}^{\mathrm{f}}(\alpha) = (1 + 2.5\alpha + 7.6\alpha^2)\left(1 - \frac{\alpha}{\alpha_{\mathrm{MX}}}\right), \tag{54}$$

$$C_{\mathrm{D}} Re^{\mathrm{s}} = \frac{4}{3} \frac{\rho^{s} d^2 g}{v_{\mathrm{t}} \mu^{\mathrm{f}} (1-\alpha)^2}, \tag{55}$$

$$g_0 = \frac{1}{1 - (\alpha/\alpha_{\mathrm{MX}})^{1/3}}, \tag{56}$$

where g is the gravitational acceleration ($g = 9.81 \text{ m s}^{-2}$). C_s in Equation (20) was set equal to zero, since in the formulation proposed by Sinclair and Jackson [39], the Reynolds stresses are neglected. Furthermore, the constitutive equations proposed by Sinclair and Jackson [39] do not include the effects of the drag force: their simplified constitutive equations can be obtained from the ones proposed in this work by simply setting $\zeta_{\mathrm{D}} = 0$ in Equation (10) for γ_{D}, in Equation (16) for μ^{s}*, and in Equation (17) for k^{s}*.

The volumetric source terms in the fluid- and solid-phase momentum equations, and in the solid-phase granular-temperature equation, were set equal to

$$S_z^{\mathrm{f}} = -\frac{\mathrm{d}P}{\mathrm{d}z}, \qquad S_z^{\mathrm{s}} = -\alpha \rho^{\mathrm{s}} g, \qquad S_r^{\mathrm{f}} = S_r^{\mathrm{s}} = S_T^{\mathrm{s}} = 0, \tag{57}$$

where $\mathrm{d}P/\mathrm{d}z$ is the overall fluid-phase reduced pressure gradient, in which the gravity term has been absorbed. This overall pressure gradient is a parameter that is specified in the 'periodic' formulation. In the 'periodic' formulation, the volume flow rates of the fluid and solid phases are not known *a priori*: they must be calculated. Therefore, an additional parameter must be prescribed in order to obtain a desired, specific, value of the ratio of the fluid-phase and solid-phase volume flow rates. This additional parameter can be one of the following: (i) the average solid-phase concentration $\bar{\alpha}$; (ii) the fluid-phase volume flow rate; (iii) the solid-phase volume flow rate; or (iv) the value of the solid-phase concentration at one point. In most of the calculations presented in this section, the solid-phase volume flow rate was considered as this additional parameter.

To complete the description of the problem, boundary conditions are required at the pipe wall. Strictly, the fluid phase must satisfy the no-slip condition, and the solid phase could undergo slip with frictional effects, at the pipe wall. Such wall boundary conditions would be appropriate if the exact local-description model were used. However, as was mentioned earlier in the paper, the exact local-description model is unsuitable for practical computations. In this work, at the wall of the pipe, the volume-averaged velocities of both the fluid and the solid

phase are assumed to be non-zero, and wall-friction effects are incorporated through the prescription of appropriate shear stresses at the wall. Sinclair and Jackson [39] used the following expression for solid-phase shear stress at the wall:

$$\sigma^{\mathrm{s}}_{rz} = -\frac{\sqrt{3T_{\mathrm{w}}}\pi\rho^{\mathrm{s}}\alpha_{\mathrm{w}}g_0}{\alpha_{\mathrm{MX}}}\frac{u^{\mathrm{s}}_{\omega}\phi'}{6}, \tag{58}$$

where ϕ' is a specularity factor that is a measure of the fraction of collisions that transfer lateral momentum to the wall. Following the approach proposed by Hui *et al.* [64], this solid-phase wall shear stress expression was obtained from the rate of transfer of lateral momentum from the particles to the wall. For specular particle–wall collisions (smooth wall), $\phi' = 0$, while for a rough wall, $\phi' = 1$. In this problem, Sinclair and Jackson used $\phi' = 0.5$.

For the fluid-phase wall shear stress, the following expression has been proposed by Sinclair and Jackson [39]:

$$\sigma^{\mathrm{f}}_{rz} = -\frac{2\mu^{\mathrm{f}}_{\mathrm{e}}\alpha_{\mathrm{MX}}T_{\mathrm{w}}u^{\mathrm{f}}_{\mathrm{w}}}{v_{\mathrm{t}}^2\alpha_{\mathrm{w}}\Delta}, \tag{59}$$

where Δ is a linear measure of the control-volume at the wall ($\Delta = \mathscr{V}_{\mathrm{cv}}^{1/3}$), and v_{t} is the terminal velocity of fall of a single particle under the influence of gravity (see Equations (52) and (55)).

The boundary condition for the granular temperature at the wall is expressed in terms of a fluctuating kinetic energy flux. Johnson and Jackson [43] have proposed an expression for this flux, obtained by assuming that the inelastic particle–wall collisions are characterized by a coefficient of restitution, e_{w}. They then used an energy balance to show that the energy flux at the wall is the sum of the rate of dissipation due to particle–wall inelastic collisions, γ_{w}, and the energy generation by slip:

$$q^{\mathrm{s}}_r = \gamma_{\mathrm{w}} + u^{\mathrm{s}}_{\mathrm{w}}\sigma^{\mathrm{s}}_{rz}, \tag{60}$$

where

$$\gamma_{\mathrm{w}} = \frac{\sqrt{3T_{\mathrm{w}}}\pi\rho^{\mathrm{s}}\alpha_{\mathrm{w}}g_0}{\alpha_{\mathrm{MX}}}\frac{(1-e_{\mathrm{w}}^2)T_{\mathrm{w}}}{4}. \tag{61}$$

In their calculations, Sinclair and Jackson used $e_{\mathrm{w}} = 0.9$.

In the 'periodic' formulation, special attention is needed to ensure that the solution will correspond to the fully-developed regime. An additional equation can be derived from the integration of the fully-developed solid-phase momentum equation in the r-direction:

$$p^{\mathrm{s}}(\alpha, T) = \text{constant} = p^{\mathrm{s}}(Q^{\mathrm{s}}). \tag{62}$$

This equation simply states that the solid-phase pressure is constant and, for the sake of concreteness in this discussion, this constant is named $p^{\mathrm{s}}(Q^{\mathrm{s}})$ and an explanation for this notation is given at the end of this paragraph. This equation relates the granular temperature T, to the solid-phase volume concentration α, through the use of Equation (12). The granular temperature is given by the solution of the fluctuating kinetic energy equation, and, therefore, for a given constant $p^{\mathrm{s}}(Q^{\mathrm{s}})$, α can be calculated at any point. The constant $p^{\mathrm{s}}(Q^{\mathrm{s}})$ in Equation (62) is prescribed so as to match the calculated solid-phase volume flow rate Q^{s}, with that computed by Sinclair and Jackson [39]: at each time step (or iteration), the solid-phase volume flow rate was computed and compared with the desired value, in order to propose a correction to the value of $p^{\mathrm{s}}(Q^{\mathrm{s}})$; and this procedure was continued until the desired solid-phase volume flow rate was obtained. This process is highly implicit and the relationship between p^{s}, α and T (Equation (12)) is non-linear. Therefore, in most of the calculations, underrelaxation was

Table II. Vertical pipe flow: comparative study

			Proposed CVFEM		Sinclair and Jackson [39]		Rel. Dif. (%)	
$d\tilde{P}/d\tilde{z}$	e	$\tilde{Q}^s$	$\tilde{Q}^f$	$\bar{\alpha}$	$\tilde{Q}^f$	$\bar{\alpha}$	$\tilde{Q}^f$	$\bar{\alpha}$
−0.2	1.0	0.34	4.4	0.19	4.4	0.18	0.0	5.6
	1.0	0.04	1.7	0.25	1.7	0.25	0.0	0.0
	1.0	−0.15	0.79	0.23	0.83	0.22	4.8	4.5
	1.0	−0.34	−0.023	0.26	−0.022	0.25	4.5	4.0
	1.0	−0.62	−0.61	0.46	−0.61	0.46	0.0	0.0
	0.99	−2.10	−2.83	0.36	−2.83	N.A.	0.0	

needed to compute α. The notation used to identify the constant in Equation (62) can now be explained: it emphasizes that this constant is indirectly prescribed by the desired solid-phase volume flow rate, Q^s.

Six cases corresponding to six different solid-phase volume flow rates were simulated in this test problem. Assuming the various physical properties given before as fixed, each case is characterized by the non-dimensional overall pressure gradient $d\tilde{P}/d\tilde{z}$, the non-dimensional solid-phase volume flow rate, $\tilde{Q}^s$, and the coefficient of restitution, e, with

$$\frac{d\tilde{P}}{d\tilde{z}} = \frac{1}{\rho^s g}\frac{dP}{dz}, \tag{63}$$

$$\tilde{Q}^s = \frac{1}{R^2 v_t}\int_0^R \alpha u^s 2\pi r \, dr. \tag{64}$$

Using a similar expression, the non-dimensional fluid-phase volume flow rate $\tilde{Q}^f$, can be calculated. Another quantity of interest that can be computed is the average solid-phase concentration, $\bar{\alpha}$. For each case, the values of $\tilde{Q}^f$ and $\bar{\alpha}$ were computed based on the solutions generated by the proposed CVFEM and compared with the values obtained by Sinclair and Jackson [39]. Table II gives the details of this comparison, including absolute values of the relative difference between the proposed solution and the results of Sinclair and Jackson [39], with the latter as the reference results. The results obtained with the CVFEM are in good agreement with the solutions of Sinclair and Jackson [39]. A grid of 3×11 was used. Eleven points were used in the r-direction in order to have a grid similar to the one used by Sinclair and Jackson [39]. In the interest of economical computations, only three points were used in the z-direction. This does not affect the accuracy of the results, since the solution is strictly one-dimensional radial. However, it should be noted that for the first case given in Table II, a grid of 11×11 was also used, and it yielded a converged solution identical to that obtained with the 3×11 grid. In the first five cases, elastic particles are involved, and a time step of the order of the particle relaxation time, τ^s_{rel}, was found to be adequate [49]. However, in the sixth case, which corresponds to inelastic particles, in order to prevent the computed solid-phase volume concentration from achieving values greater than the corresponding value at maximum packing, it was necessary to use $\Delta t \leq \tau^s_{rel}/10$.

As was stated before, $\tilde{Q}^s$ was used as the additional parameter in the 'periodic' formulation. However, in order to obtain results comparable with those of Sinclair and Jackson [39], in the third case, the centerline solid-phase concentration was used as the additional parameter, so there is a small difference in the corresponding solid-phase volume flow rates: the proposed

CVFEM predicted $\tilde{Q}^s = -0.15$, while for the corresponding case in Sinclair and Jackson [39], $\tilde{Q}^s = -0.16$.

The detailed CVFEM results, consisting of the axial velocity, concentration, and granular-temperature profiles, corresponding to the fifth and sixth cases described in Table II, are presented in Figures 5 and 6. For the fifth case, a simulation with 21 points in the r-direction was also undertaken, and the resulting solution was found to be so close to the 11-point solution that the respective curves presented on plots similar to Figure 5 were indistinguishable.

The first five cases of this problem correspond to idealized conditions where the coefficient of restitution for particle–particle collisions is set equal to unity ($e = 1$) and the effects of the drag force in the constitutive equations are assumed negligible (this is obtained by setting $\zeta_D = 0$ in Equation (10) for γ_D, in Equation (16) for μ^{s*}, and in Equation (17) for k^{s*}). For these idealized conditions, using Equations (1)–(18) and the specializations given in Table I for the granular temperature T, it can be established that at the centerline of the pipe, $r/R = 0$, T can take on *any* finite value, and $\partial T/\partial r = 0$. This feature is clearly seen in the plot of T/v_t^2

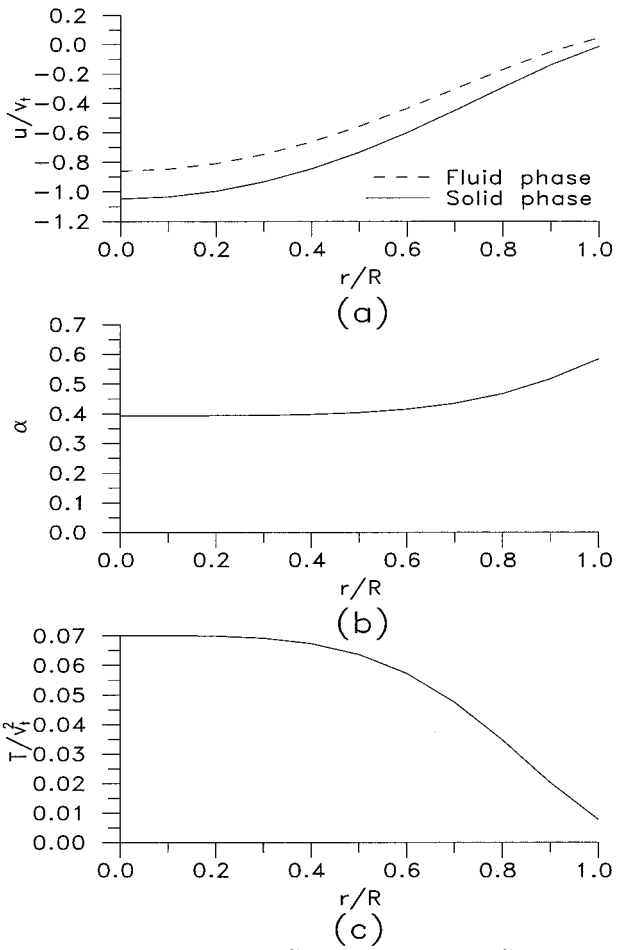

Figure 5. Vertical pipe flow: $d\tilde{P}/d\tilde{z} = -0.2$; $e = 1.0$; $\tilde{Q}^s = -0.62$.

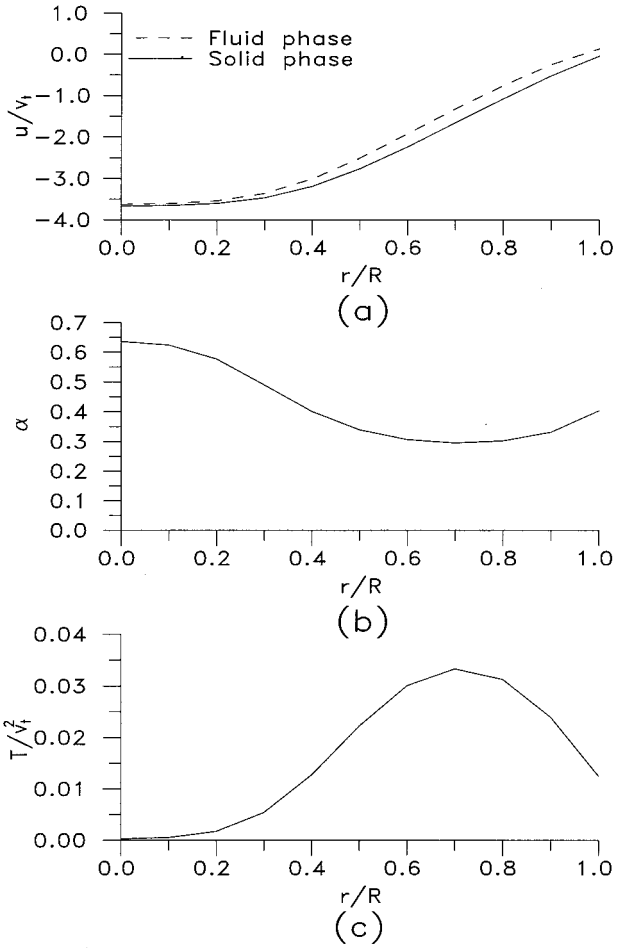

Figure 6. Vertical pipe flow: $d\tilde{P}/d\tilde{z} = -0.2$; $e = 0.99$; $\tilde{Q}^s = -2.10$.

versus r/R in Figure 5, which corresponds to Case 5. However, when $e < 1$ or $\zeta_D \neq 0$, the physically realistic condition of $T = 0$ is achieved at the centerline, $r/R = 0$. This feature is evident in the T/v_t^2 versus r/R plot in Figure 6, which corresponds to Case 6 where $e = 0.99$ (see Table II).

In all the simulations, there is a region of high concentration near the wall, because the particle–wall inelastic collisions have the effect of accumulating particles in the vicinity of the wall. In the case of inelastic particle–particle collisions (Case 6, Figure 6), the concentration profile presents a different behavior than the other cases: the maximum concentration is at the center of the pipe. This migration of the particles to the center of the pipe, which is ascribed to shear-induced particle migration in the literature [65], is in qualitative agreement with experiments [66] and Stokesian dynamics simulations [44]. In these studies, a flattening of the velocity profiles in the vicinity of the centerline was also observed. Again, such a flattening behavior can be noted in the CVFEM solution corresponding to the case of particle–particle inelastic collisions (Figure 6(a)). The shape of the velocity profiles and the direction of the particle migration confirm that the migration goes from high to low shear-rate regions [65].

The physical mechanism that explains such a migration is still not well understood [44]. Leighton and Acrivos [65] suggested that the migration is due to the roughness of the particles; Nott and Brady [44] explained this behavior by the chaotic motion that takes place in a system of more than three particles. Based on the results of this section, all that can be said for certain is that inelastic collisions between the particles clearly induce particle migration to the center of the pipe.

4.2. Flow in an annular shear cell apparatus

Total normal and shear stresses in gas–solid particle flows have been obtained experimentally by Savage and Sayed [67], and Hanes and Inman [68], using an annular shear cell apparatus. These experiments provide data that can be used to examine the various mathematical descriptions of the fluid- and solid-phase stress tensors. Savage and Sayed [67] used polystyrene beads, glass beads, and crushed walnut in air. Hanes and Inman [68] used glass beads in air and water. These experiments can be described by the simple plane shearing model of Figure 7 if the centrifugal effects are negligible. In the experiments of Savage and Sayed, for example, the centrifugal effects modify the solid-phase stresses by only 1–2% [67]. Using this assumption, Johnson and Jackson [43] have solved this problem with the simple plane shearing model. The stress model used in their analysis includes both collisional and frictional contributions. The frictional contribution appears at dense concentrations, close to the maximum packing of the granular material, when particles interact with each other through long-term direct contact. Their evaluation of the frictional contribution included an empirical constant which was calculated to fit the experimental data. Another adjustable parameter was also included in their collisional contribution. Only comparisons with the experimental data of Savage and Sayed [67] are presented in the work of Johnson and Jackson [43].

In this section, numerical solutions of the simple plane shearing model obtained using the proposed CVFEM are compared with some of the experimental data of Savage and Sayed [67] and Hanes and Inman [68]. As stated earlier, the frictional contribution becomes significant only when the concentration is close to the maximum packing of the granular material. At lower concentrations, frictional contribution can also become important when the shearing of the material is very low. In this section, only the relatively high shearing experiments at concentrations far from the close-packing concentration will be presented. No comparison with the numerical solutions of Johnson and Jackson [43] will be presented, since the mathematical model used in this work does not include any frictional contribution to the solid-phase stress tensor.

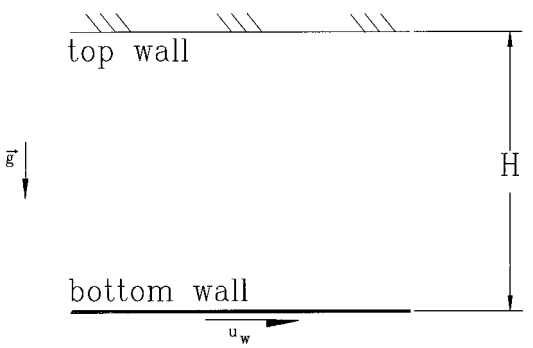

Figure 7. Plane shearing model.

The plane shearing problem solved in this section consists of a fixed top wall and a moving bottom wall separated by a distance H, as shown in Figure 7. The velocity of the bottom wall is denoted as u_w and is in the positive x-direction. The bottom wall is located at $y = 0$, and the top wall is located at $y = H$. The experiments of Savage and Sayed [67], and Hanes and Inman [68] were designed to give the normal and shear stresses at the top wall.

Strictly, this problem is one-dimensional, but in order to test the proposed two-dimensional formulation, a finite length of the plane shearing cell is modelled along with periodic boundary conditions at the inlet and outlet planes of the calculation domain.

The experiments of Savage and Sayed [67], and Hanes and Inman [68] were constructed to minimize the slip of the solid phase at the top and bottom walls of the annular shearing cell: Savage and Sayed used sand paper, while Hanes and Inman cemented a layer of solid particles on each wall. The type of surface roughness used by Hanes and Inman ensures a perfect no-slip condition of the solid phase. With the sand paper, a slip can exist, and, therefore, the slip boundary conditions proposed by Sinclair and Jackson [39] were used. Particle–wall collisions were assumed inelastic. In this work, the granular-temperature gradients at the walls were prescribed following the analysis proposed by Sinclair and Jackson [39].

As was the case in the 'periodic' formulation of the flow in a vertical pipe, an additional equation is needed to converge to the desired fully-developed solution. This equation was obtained by the integration of the solid-phase momentum equation in the y-direction, and is used to select an appropriate solid-phase average concentration, $\bar{\alpha}$:

$$p^s(\alpha, T) = \left[p^s(\bar{\alpha}_{EXP}) - (\rho^s - \rho^f) g \int_0^y \alpha \, dy \right], \tag{65}$$

where $p^s(\bar{\alpha}_{EXP})$ is a constant which has to be prescribed in order to ensure that at convergence, the average volume concentration calculated by the CVFEM corresponds to the experimental one after each time step (or iteration); the average volume concentration of the CVFEM solution, $\bar{\alpha}_{CVFEM}$, was computed. Then, $p^s(\bar{\alpha}_{EXP})$ was modified so as to meet the requirement that $\bar{\alpha}_{CVFEM}$ should be equal to the average volume concentration of the experiment, $\bar{\alpha}_{EXP}$. The average concentration was computed using the integrated solid-phase y-momentum equation (Equation (65)). This process is highly implicit, and it was necessary to underrelax α during the solution process in order to ensure convergence.

The geometrical and physical parameters of the various simulations presented in this section are given in Table III. All the simulations were performed for the case of glass particles in air. To simulate the experiments of Hanes and Inman [68], the coefficients of restitution, e and e_w, were set to 0.95. This is the value of the coefficient of restitution of glass particles, e, in a vacuum [42]. For the simulation corresponding to the experiments of Savage and Sayed [67], smaller values of e and e_w were used. The smaller value of e_w is justified due to the type of wall surfaces used in their experiment, namely, sandpapered wall. For such a surface, Johnson and Jackson [43] have suggested $e_w = 0.50$ and $\phi' = 0.60$. The use of a smaller e, however, needs more justifications. It is assumed that the sandpapered surfaces scratched the glass particles. Lun and Savage [69] showed that rough particles tend to have more rotational energy than smooth particles, and this, in turn, leads to lower levels of stresses. In the mathematical model proposed in this work, the particles are assumed to be smooth and, therefore, no rotational energy is included in the analysis. A parametric study of some of the various parameters appearing in the proposed theory was undertaken in order to choose appropriate values of e.

The results of the parametric study are presented in Figure 8 for a case corresponding to an experiment of Savage and Sayed [67]. Figure 8(a) illustrates the effect of the coefficient of

Table III. Flow in annular shear cell: various parameters

Experiment	$\bar{\alpha}$	d (mm)	ρ^s (kg m^{-3})	H (mm)	e	e_w	ϕ'
Savage and Sayed [67]	0.477	1.80	2970	11.610	0.89	0.50	0.60
	0.507	1.80	2970	10.920	0.89	0.50	0.60
Hanes and Inman [68]	0.440	1.85	2780	13.717	0.95	0.95	–
	0.460	1.85	2780	13.121	0.95	0.95	–
	0.490	1.85	2780	12.317	0.95	0.95	–

restitution of the particle–particle collisions, e, on the non-dimensionalized total shear and normal stresses at the top wall:

$$\tau_s^* = \frac{\tau_s}{\rho^s g d}, \qquad \tau_n^* = \frac{\tau_n}{\rho^s g d}, \tag{66}$$

where τ_n and τ_s are the sum of the solid- and fluid-phase stresses applied normally and tangentially to the top wall, respectively. Only the results with $e > 0.8$ are presented, since the

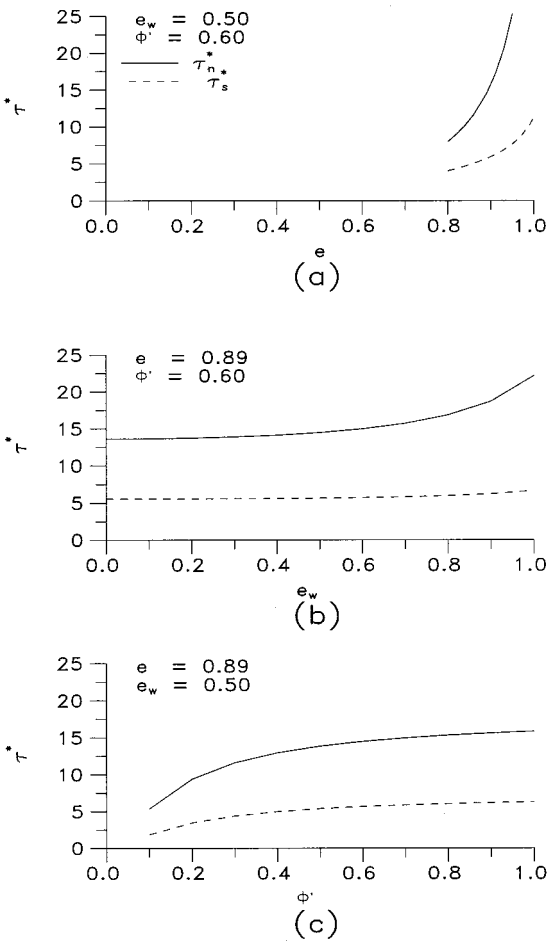

Figure 8. Parametric study of flow in annular shear cell: $\bar{\alpha} = 0.477$; $(d/g)^{1/2}(u_w/H) = 2.0$.

theory is only applicable for slightly inelastic particles. As is clearly seen, there is a significant decrease of the shear and normal stresses as the coefficient of restitution, e, decreases. A variation of 70% is noted between the computed normal stresses corresponding to $e = 0.95$ and 0.80: the corresponding variation of the shear stress is 50%. This behavior is associated with the dissipation of fluctuating energy by inelastic collisions, which results in a lower level of granular temperature and, therefore, in smaller values of the solid-phase stresses. These important variations of the stresses illustrate that physically meaningful simulations can be realized only when a good evaluation of e is available. In order to obtain a comparable level of stresses between the experiments of Savage and Sayed [67] with rough particles and the smooth-particle simulations performed with the proposed CVFEM, a smaller value of e ($= 0.89$) than the one corresponding to glass particles in a vacuum ($e = 0.95$) was used in the CVFEM simulations.

A parametric study was also undertaken to quantify the effects of e_w and ϕ' (see Figure 8(b,c)). The influence of e_w is similar to that of e, but with much smaller variations: between $e_w = 1.0$ and 0.0, a variation of 40% is noted on the normal stress and 20% on the shear stress. Furthermore, most of the variation is noted in the range $0.8 < e_w < 1.0$. The effect of the specularity coefficient ϕ' is illustrated in Figure 8(c): there is an increase of the shear and normal stresses as ϕ' increases. Low values of ϕ' correspond to smooth walls, while large values correspond to rough walls. Rough walls produce solid-phase fluctuating kinetic energy and, therefore, the solid-phase stresses increase. Another parameter which significantly influences the level of stress is the radial distribution function g_0. In the present simulations, the radial distribution function was taken as

$$g_0 = \frac{1}{1 - (\alpha/\alpha_{MX})^{1/3}}, \tag{67}$$

with $\alpha_{MX} = 0.65$. The radial distribution function proposed by Lun [42] (Equation (18)), produces a decrease of 20% in the stress level.

Figure 9 presents fluid- and solid-phase velocity, solid-phase volume concentration, and granular-temperature profiles for the same problem as that corresponding to Figure 8, but with specific values of e, e_w and ϕ': $e = 0.89$, $e_w = 0.50$ and $\phi' = 0.6$. The fluid and solid phases are in dynamic equilibrium in almost the entire domain: only slight differences in velocity are noted in regions near the walls. It is also seen that the velocity profiles are not linear, as is the case in the single-phase Couette flow. The concentration profile exhibits an accumulation of particles near both the bottom and top walls. The increase in concentration at the bottom is explained by the action of gravity which tends to accumulate particles at the bottom of the shear cell. The migration of particles to the region near the top wall is induced by the inelastic wall–particle collisions. The granular-temperature profile shows strong increases of T near the walls, which illustrates that the production of solid-phase fluctuating energy by rough walls is more important than the dissipation by inelastic particle–wall collisions.

Comparisons of the experimental normal and shear stresses with those obtained using the proposed mathematical model are presented in Figures 10 and 11. Figure 10 presents a comparison with the results of Savage and Sayed [67] for glass particles of 1.80 mm diameter, and the results in Figure 11 show a comparison with the experimental results of Hanes and Inman [68] for glass particles of 1.85 mm diameter. The experimental and numerical results show fair agreement, with the shear stresses showing a better agreement (see Figure 10(a) and Figure 11(a)) than the normal stresses (see Figure 10(b) and 11(b)). Furthermore, the overall trends, in terms of variation with the apparent shear rate, $(d/g)^{1/2}(u_w/H)$, and average concentration, $\bar{\alpha}$, are well predicted.

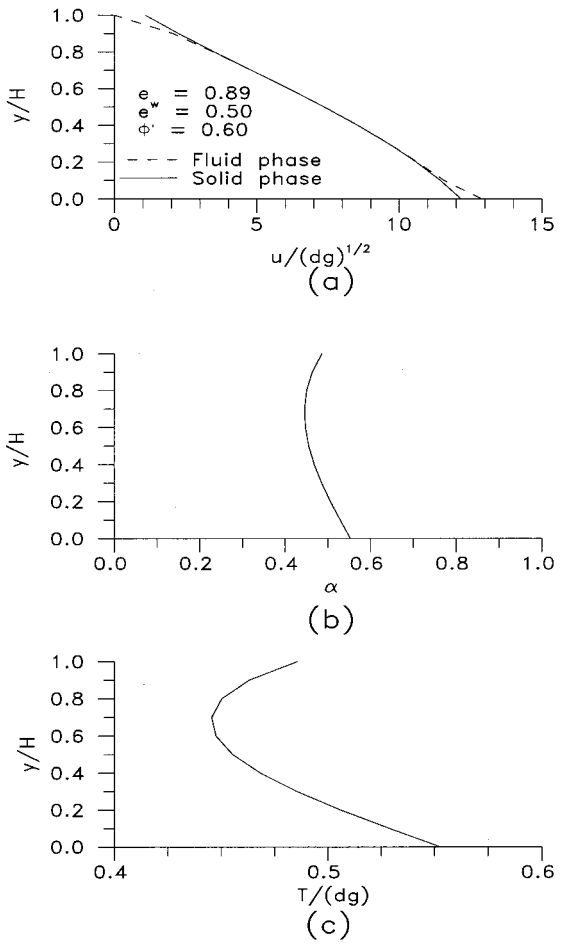

Figure 9. Velocity, concentration and temperature profiles for flow in annular shear cell: $\bar{\alpha} = 0.477$; $(d/g)^{1/2}(u_w/H) = 2.0$.

In conclusion, it should be noted that the experiments of Savage and Sayed [67] and those of Hanes and Inman [68] were done with similar particles, however, the stresses measured by the former are much smaller that those obtained by the latter. This discrepancy is attributed to the different types of wall roughness used in each experiment [68]. As was stated earlier, Hanes and Inman used a cemented layer of particles, and, therefore, ensured the applicability of the non-slip condition at the wall. Savage and Sayed used sandpaper at the wall, which only reduces the slip, and transforms the smooth particles into rough particles.

4.3. Flow in a channel with a restriction

Dilute gas–solid particle flows in a channel with a restriction has been analyzed recently using a dilute-concentration model [48]. A schematic illustration of this problem is given in Figure 12. Here, the granular-temperature model is used to investigate this problem. The use of this general mathematical model for a gas–solid particle flow of dilute concentration is computationally inefficient, since an additional equation, namely the fluctuating kinetic energy

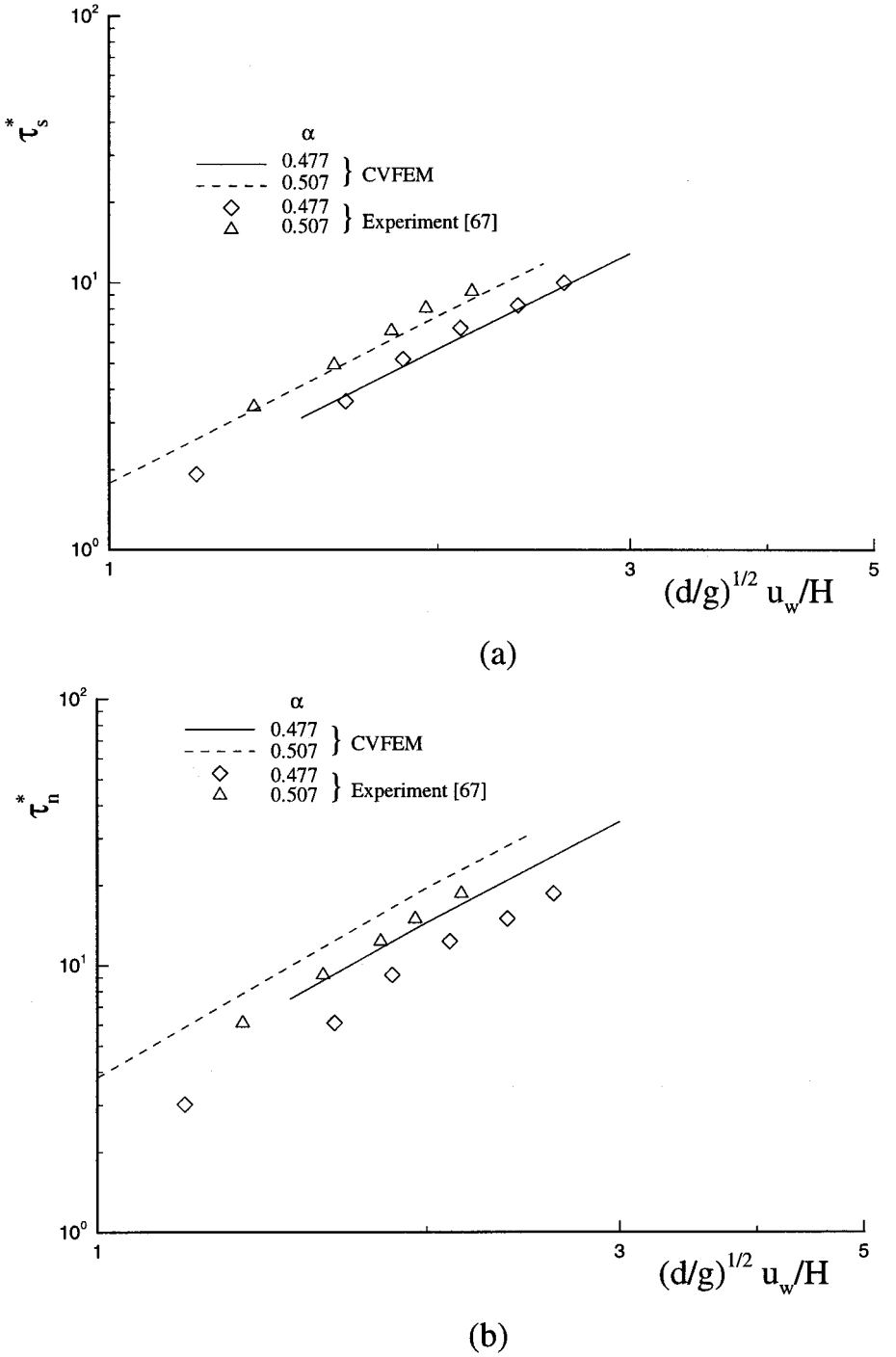

Figure 10. Shear and normal stresses for flow in annular shear cell: $e = 0.89$; $e_w = 0.50$; $\phi' = 0.60$.

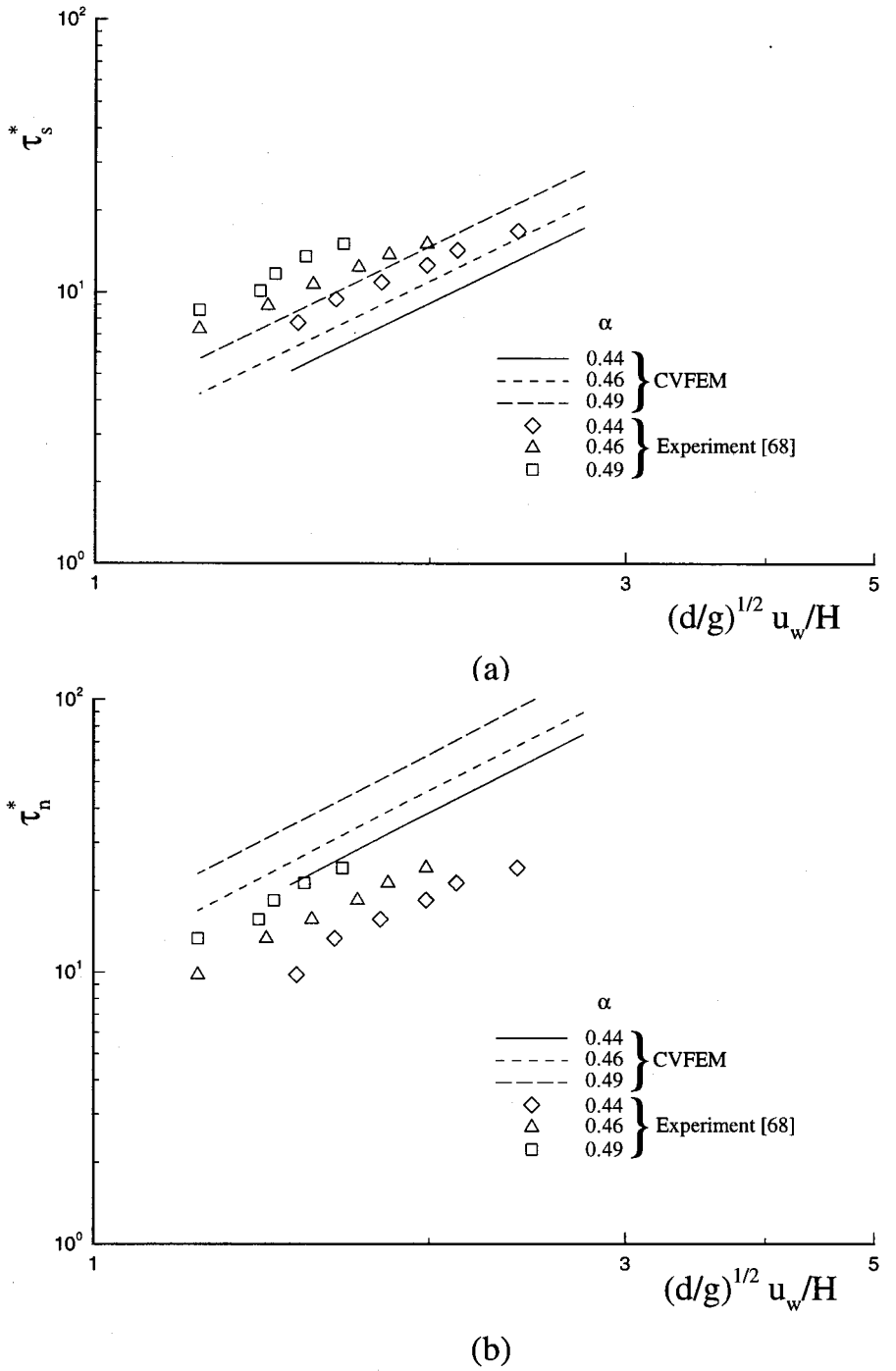

Figure 11. Shear and normal stresses for flow in annular shear cell: $e = 0\ 95$; $e_w = 0.95$; no-slip.

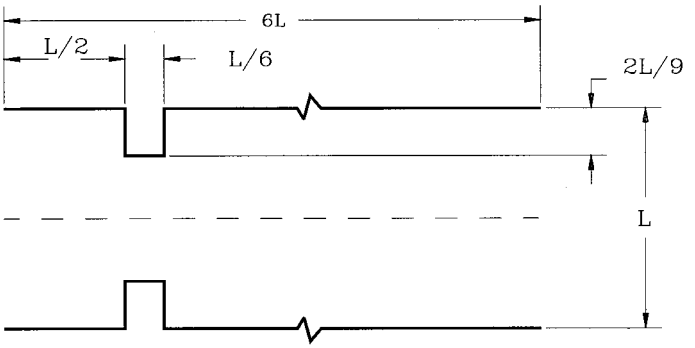

Figure 12. Geometry of the channel with a restriction.

equation, needs to be solved. However, this test provides an assessment of the validity of the general mathematical model in the simulation of gas–solid particle flows of dilute concentration. It is necessary to demonstrate this feature of the general mathematical model, before it can be used with confidence in the simulation of gas–solid particle flows that involve a wide range of the solid-phase volume concentration.

The boundary conditions are the same as those used in the corresponding problem described in Reference [48]: (i) uniform inlet profile for α; (ii) identical Poiseuille inlet velocity profiles for both phases; (iii) outflow treatment at the outlet plane; (iv) no-slip condition at the walls for the fluid phase; and (iv) *slip* condition at the walls for the *solid phase*. It should be noted that these boundary conditions are equivalent to stating that the wall is smooth, or $\phi' = 0$. In addition, the boundary conditions and parameters related to the granular temperature are: (i) zero granular temperature at the inlet plane; (ii) inelastic particle–wall collisions, with $e_w = 0.9$; and (iii) outflow treatment at the outlet planes. The coefficient of restitution for particle–particle collisions, e, is assumed to be 0.9.

The values of the various parameters in this problem are presented in Table IV. Here, the Reynolds number is defined as $Re = \rho^f u_{cl}^f L/\mu^f$, where u_{cl}^f is the fluid-phase centerline velocity component in the axial direction at the inlet plane; the Stokes number is $Sk = \tau^s/\tau^f$, with $\tau^s = 4/3(\rho^s d^2/\mu^f C_D Re^s)$, $C_D Re^s = 24 + 4(Re^s)^{2/3}$ and $\tau^f = L/u_{cl}^f$; and $\gamma = \rho^s/\rho^f$. Figures 13–16 present the solutions obtained with the dilute concentration model [48] and the general granular-temperature model. All of these results were obtained using a 73×37 grid. At a Stokes number of $Sk = 10^{-2}$, the solutions are in very good agreement for both $\alpha_{in} = 10^{-3}$ and 5×10^{-3}. The results for $Sk = 10^{-1}$ and $\alpha_{in} = 5 \times 10^{-3}$ also compare very well. These successful comparisons demonstrate the validity of the general mathematical model in the dilute concentration regime. At $Sk = 10^{-1}$ and $\alpha_{in} = 5 \times 10^{-3}$, there is a minor discrepancy in the results: the fluid-phase pressure drop (Figure 15), predicted by the general model is slightly larger than that obtained with the dilute concentration model. This may be due to the

Table IV. Values of parameters for flow in a channel with a restriction

Re	*Sk*	α_{in}	γ
100	10^{-2}	10^{-3}	1000
100	10^{-2}	5×10^{-3}	1000
100	10^{-1}	5×10^{-3}	1000

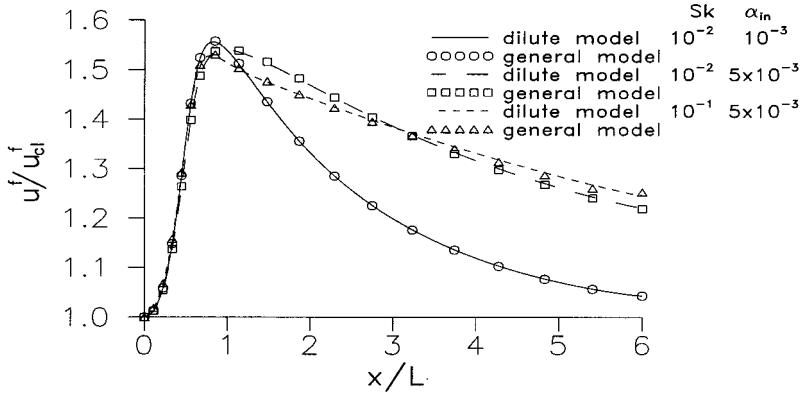

Figure 13. Flow in a channel with a restriction: variation of fluid-phase velocity along the centerline.

increasing effects of the particle–particle collisions. For this relatively large value of the Stokes number, the solid phase is not necessarily in dynamic equilibrium with the fluid phase: therefore, the solid-phase concentration could build up in certain regions, such as near the walls, and the effects of the particle–particle collisions could become significant.

4.4. Split-flow inertial separator

In an earlier paper [48], dilute gas–solid particle flows in an idealized, laminar split-flow inertial separator were analyzed using a dilute-concentration mathematical model. A schematic illustration of this problem is given in Figure 17. The ratio of the inlet external radius, R_e, to the inlet internal radius, R_i, is equal to 2. The other geometric parameters may be obtained from Figure 17, since this figure is drawn to scale. In this paper, the general granular-temperature model is used to investigate this problem. The separator contains regions of low and high volume concentration of the solid phase. At the inlet and in the main duct, the solid-phase concentration is relatively low. However, when the separator is operating at high efficiency, the solid-phase concentration in the bypass duct may reach values at which the effects of the

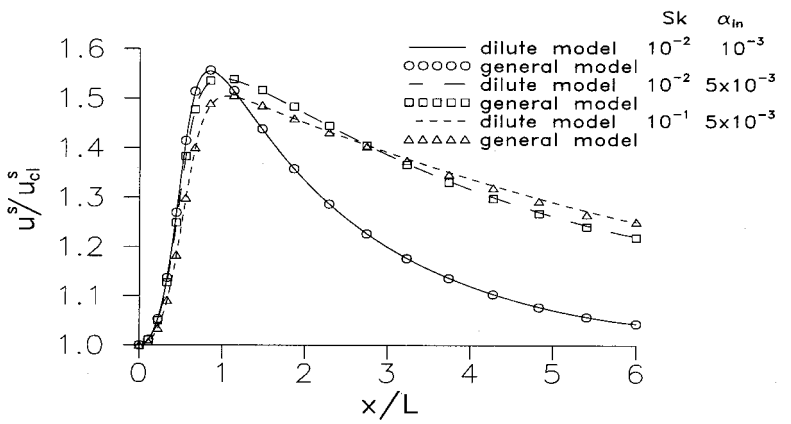

Figure 14. Flow in a channel with a restriction: variation of solid-phase velocity along the centerline.

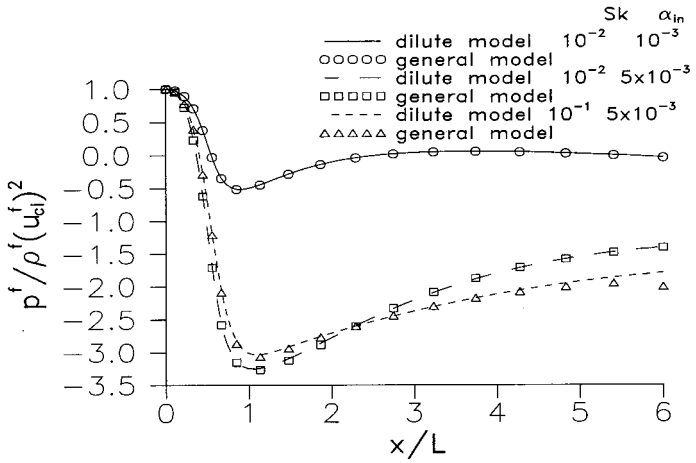

Figure 15. Flow in a channel with a restriction: variation of fluid-phase pressure along the centerline.

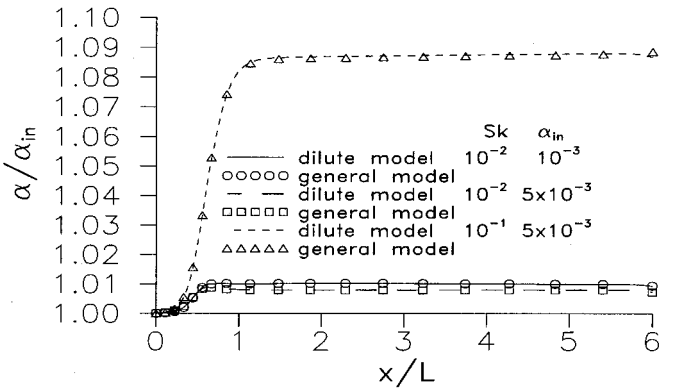

Figure 16. Flow in a channel with a restriction: variation of solid-phase concentration along the centerline.

particle–particle collisions are no longer negligible. The effects of such collisions in the split-flow inertial separator can be illustrated by a comparison between solutions obtained with the dilute-concentration model [48] and the general granular-temperature model presented in this work.

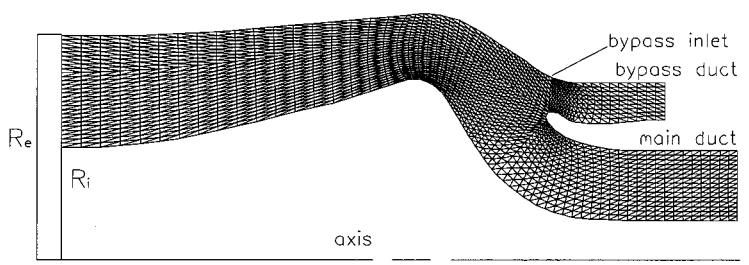

Figure 17. Geometry of the separator.

The following boundary conditions were used with this model:

- Fluid phase
  - Prescribed uniform axial velocity and zero radial velocity at the inlet.
  - Outflow treatment [45] at the outlet planes for all the fluid-phase dependent variables.
  - No-slip condition at the wall.
- Solid phase
  - Prescribed concentration, uniform axial velocity, zero radial velocity, and zero granular temperature at the inlet plane.
  - Outflow treatment [45] at the outlet planes for all the solid-phase dependent variables.
  - Inelastic particle–wall collisions on a smooth wall: $e_w = 0.9$ and $\phi' = 0$.

The assumption of smooth wall leads to solid-phase slip condition at the wall (zero shear stress): this assumption also ensures that the boundary conditions of the general model are similar to the ones of the dilute-concentration model [48]. The coefficient of restitution for particle–particle collisions, e, is assumed to be 0.9.

The non-dimensional parameters that govern the fluid flow in this problem are the Reynolds number, Re, based on the inlet hydraulic diameter ($D_H = 2(R_e - R_i)$) and the prescribed uniform axial velocity, u_{in}^f, of the fluid phase at the inlet; the Stokes number, $Sk = \tau^s/\tau^f$ with $\tau^s = \frac{4}{3}(\rho^s d^2/\mu^f C_D Re^s)$, $C_D Re^s = 24 + \frac{18}{5}(Re^s)^{0.687}$, and $\tau^f = D_H/u_{in}^f$; $\gamma = \rho^s/\rho^f$, the ratio of the densities of the solid and fluid phases; the inlet volume concentration of the solid phase, α_{in}; and the bypass ratio, b. The bypass ratio, b, defined as the ratio of the fluid-phase mass flow rate through the bypass duct to the fluid-phase inlet mass flow rate, is controlled by the pressure difference between the main-duct outlet plane and the bypass outlet plane. All the simulations in this comparative study were done with $Re = 200$, $b = 20\%$, $\gamma = 1000$, and $\alpha_{in} = 10^{-3}$. These results were obtained using the grid illustrated in Figure 17. The influence of the Stokes number was investigated in the range $10^{-3} \leq Sk \leq 10^{-1}$.

Figure 18(a) gives the variation of the separator efficiency, η_{ef}, as a function of the Stokes number, Sk. The separator efficiency η_{ef} indicates, for a given bypass ratio, b, the effectiveness of a given separator. This efficiency is defined as the ratio of the solid-phase mass flow rate through the bypass duct to the solid-phase inlet mass flow rate. The solid line corresponds to the solution of a dilute concentration model [48] and the dashed line represents the solution of the granular-temperature model. At large Sk, the dilute-concentration model overestimates the separator efficiency, and the difference between the two models reaches a maximum value of 52%. Whenever there is a build up in the concentration of particles, the collisions tend to spread out the particles: thus the effect of collisions is to make the solid-phase concentration more uniform, and decrease the separator efficiency.

The variation of the non-dimensionalized fluid-phase static-pressure drop in the main duct, Δp_M^{f*}, with Stokes number, Sk, is presented in Figure 18(b). Δp_M^{f*} is defined as

$$\Delta p_M^{f*} = \frac{p_{in,c}^f - p_{out,M}^f}{0.5\rho^f (u_{in}^f)^2}, \tag{68}$$

where $p_{in,c}^f$ is the static pressure at the central node in the inlet plane of the separator; $p_{out,M}^f$ is the static pressure at the outlet plane of the main duct; ρ^f is the density of the fluid phase; and u_{in}^f is the prescribed uniform velocity of the fluid phase at the inlet plane of the separator. The results obtained with the dilute-concentration and general models show similar behavior. Δp_M^{f*} asymptotes to the homogeneous-mixture solution as Sk decreases, at low values of Sk. A decrease of Δp_M^{f*} with increasing Sk, at large Sk, is also evident. At an intermediate value of Sk, there is a maximum. However, this maximum does not appear at the same Sk for each

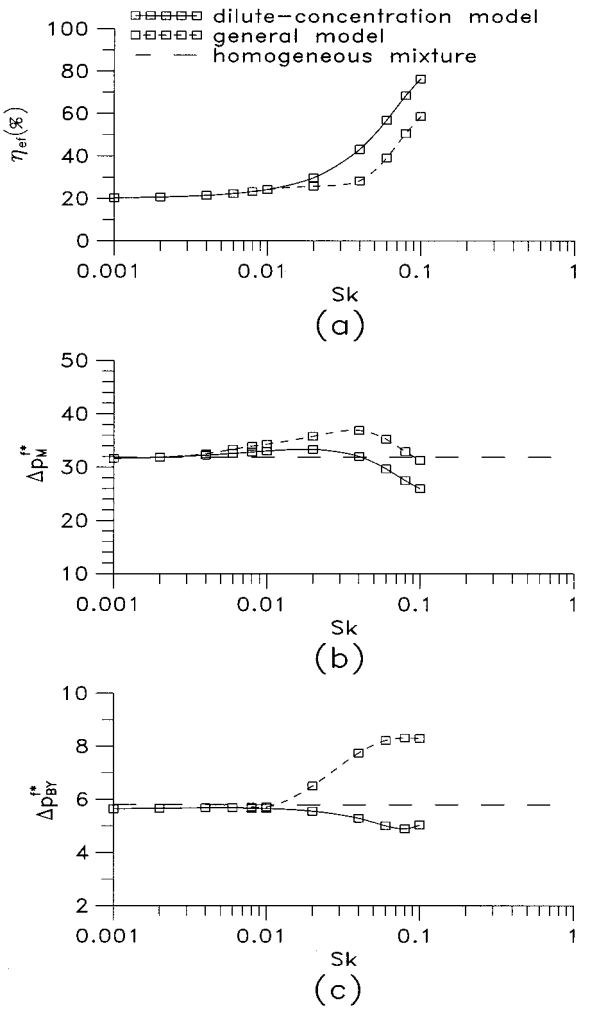

Figure 18. Results pertaining to $b = 20\%$, $\gamma = 10^3$ and $\alpha_{in} = 10^{-3}$: (a) separator efficiency; (b) static-pressure drop in the main duct; (c) static-pressure drop in the bypass duct.

model: the granular-temperature model predicts the maximum at a larger *Sk* than the corresponding value for the dilute concentration model. Furthermore, Δp^{f*}_{M} estimated with the granular-temperature model is always greater than that predicted using the dilute-concentration model: particle–particle collisions lead to a viscosity of the solid phase and the associated stresses, and, therefore, a larger fluid-phase pressure drop is needed to drive the same mass of mixture. The increase in pressure drop is more pronounced at high *Sk*. This is to be expected since the relaxation time of a particle increases with increasing *Sk*, while the frequency of collisions is essentially constant for a given inlet concentration. It is also seen that the effects of the collisions are much stronger on the non-dimensionalized fluid-phase static-pressure drop in the bypass duct, Δp^{f*}_{BY}, (see Figure 18(c)). In this figure, Δp^{f*}_{BY} is defined as

$$\Delta p^{f*}_{BY} = \frac{p^{f}_{in,c} - p^{f}_{out,BY}}{0.5\rho^{f}(u^{f}_{in})^2}, \tag{69}$$

where $p^{f}_{out,BY}$ is the static pressure at the outlet plane of the bypass duct. With the granular-temperature model, as Sk increases, Δp^{f*}_{BY} does not decrease, as predicted by the dilute-concentration model, but increases due to the increasing effects of the particle–particle collisions. Furthermore, this increase is amplified by the combined effects of the increasing Sk and increasing solid-phase concentration (associated with the increase in the efficiency). Again, at low Sk, the results of both models asymptote to the homogeneous-mixture solution.

These results show that even at relatively low values of inlet concentrations, α_{in}, the effects of the collisions may not be negligible. This is especially true at large values of the Stokes number and in regions where there is a build up of solid-phase concentration, such as in the bypass duct. These results also clearly illustrate that a mathematical model that includes particle–particle collisions is essential for accurate solutions of gas–solid particle flow problems involving a wide range of solid-phase concentrations. Finally, the results of this problem demonstrate that the proposed CVFEM can be successfully used to simulate gas–solid particle flows in complex geometries, over a wide range of the solid-phase concentration.

5. CONCLUSION

The main contributions of this work are the presentation of a granular-temperature model and the development of a CVFEM for the solution of dense gas–solid particle flows in irregular-shaped geometries. The granular-temperature model is a simplified version of a model proposed by Lun and Savage [5,42]. The mathematical model and the proposed CVFEM have been applied to three test problems and one demonstration problem. The results are quite encouraging.

ACKNOWLEDGMENTS

The support of the Natural Sciences and Engineering Research Council of Canada (NSERC), in the form of a Postgraduate Scholarship to C. Masson and a Research Grant to B.R. Baliga, is gratefully acknowledged. We are also grateful to Fonds pour la formation de Chercheurs et l'Aide à la Recherche (FCAR) and McGill University for support to C. Masson in the form of Postgraduate Scholarships. We would like to thank the reviewers of this paper for their detailed comments and constructive criticism.

APPENDIX A. NOMENCLATURE

ac^{p}_{i}, ac^{p}_{nb}, b^{p}	coefficients in the algebraic, discretized, equation for p^{f} [ms]
ac^{T}_{i}, ac^{T}_{nb}, b^{T}	coefficients in the algebraic, discretized, granular-temperature equation [kg s^{-1}]
ac^{u}_{i}, ac^{u}_{nb}, b^{u}	coefficients in the algebraic, discretized, z-momentum equation [kg m^{-1}]
ac^{v}_{i}, ac^{v}_{nb}, b^{v}	coefficients in the algebraic, discretized, r-momentum equation [kg m^{-1}]
ac^{α}_{i}, ac^{α}_{nb}, b^{α}	coefficients in the algebraic, discretized, equation for α [kg s^{-1}]
A, B, C	coefficients in the interpolation function for ϕ
C_{D}	particle drag coefficient (Equation (18))
C_{s}	constant appearing in the evaluation of the Reynolds stress (Equation (20)) [$s^{1/2}$]
d	particle diameter [m]

d^{f}, e^{f}, f^{f}	coefficients in the interpolation function for the fluid-phase pressure
d^{s}, e^{s}, f^{s}	coefficients in the interpolation function for the solid-phase pressure
$d^{u\mathrm{f}}$	pressure-gradient coefficient for u [$\mathrm{m^3\ s\ kg^{-1}}$]
$d^{v\mathrm{f}}$	pressure-gradient coefficient for v [$\mathrm{m^3\ s\ kg^{-1}}$]
e	coefficient of restitution for particle–particle collisions
e_{w}	coefficient of restitution for particle–wall collisions
f^+, f^-	mass-weighted functions (Equations (33)–(35))
g	gravitational acceleration ($=9.81$ m $\mathrm{s^{-2}}$)
g_0	equilibrium radial distribution function (Equation (18))
$\vec{i}, \vec{j}$	units vectors in the z- and r-direction, respectively
$\vec{J}$	combined convection–diffusion flux of ϕ (Equation (24))
$\vec{J}_D$	diffusion flux of ϕ (Equation (25))
$\vec{J}_C$	convection flux of ϕ (Equation (26))
k^{s}_T	diffusion coefficient related to granular-temperature gradient (Equation (14)) [$\mathrm{N\ s\ m^{-2}}$]
k^{s}_α	diffusion coefficient related to solid-phase volume concentration gradient (Equation (15)) [$\mathrm{N\ s^{-1}}$]
$\dot{m}$	mass flow rate [$\mathrm{kg\ s^{-1}}$]
$\dot{M}$	material mass flow rate [$\mathrm{kg\ s^{-1}}$]
$\vec{n}$	unit normal vector
p	pressure, [Pa]
Q^{s}, Q^{f}	volume flow rates of the solid and fluid phases, respectively [$\mathrm{m^3\ s^{-1}}$]
$\tilde{Q}^{\mathrm{s}}$, $\tilde{Q}^{\mathrm{f}}$	non-dimensional volume flow rates of the solid and fluid phases, respectively
r	radial co-ordinate in the cylindrical-polar co-ordinate system, [m]
Re	Reynolds number
Re^{s}	particle Reynolds number ($=\rho^{\mathrm{f}} d\lvert\vec{V}^{\mathrm{s}}-\vec{V}^{\mathrm{f}}\rvert/\mu^{\mathrm{f}}$)
s	length [m]
Sk	Stokes number
S	volumetric source term for ϕ
t	time [s]
T	granular temperature [$\mathrm{m^2\ s^{-2}}$]
u	velocity component in the z-direction [$\mathrm{m\ s^{-1}}$]
$\hat{u}_i$	z-component of the pseudo-velocity at node i [$\mathrm{m\ s^{-1}}$]
v	velocity component in the r-direction [$\mathrm{m\ s^{-1}}$]
$\hat{v}_i$	r-component of the pseudo-velocity at node i [$\mathrm{m\ s^{-1}}$]
v_{t}	terminal velocity of fall of a single particle under gravity [$\mathrm{m\ s^{-1}}$]
$\mathscr{V}$	volume [$\mathrm{m^3}$]
W_p	solid-phase pressure work source term (Equation (8)) [$\mathrm{W\ m^{-3}}$]
x	local co-ordinate in the direction of z (Figure 3(a)) [m]
y	local co-ordinate in the direction of r (Figure 3(a)) [m]
z	axial co-ordinate in the cylindrical-polar co-ordinate system [m]

Greek Symbols

α	solid-phase volume concentration
β	volume concentration in general governing equation (Equation (1))
Δ	linear measure of the grid size [m]
Δt	time step [s]

ϵ	fluid-phase volume concentration
ζ_D	specific fluid friction coefficient (Equation (9)) [kg m s^{-3}]
η	coefficient related to e (Equation (18))
γ	density ratio ($=\rho^s/\rho^f$)
γ_c	solid-phase fluctuating kinetic energy dissipation due to inelastic collisions (Equation (9)) [W m^{-3}]
γ_B	solid-phase fluctuating kinetic energy transfer term (Equation (10)) [W m^{-3}]
γ_D	solid-phase fluctuating kinetic energy dissipation due to drag (Equation (10)) [W m^{-3}]
Γ_b	bulk diffusion coefficient for ϕ (Equations (2)–(4); Table I)
Γ_e	effective diffusion coefficient for ϕ (Equations (1)–(4); Table I)
μ^f	dynamic viscosity of the fluid phase [Ns m^{-2}]
μ_e	effective viscosity (Equations (13) and (19)) [Ns m^{-2}]
μ_b	bulk viscosity (Equations (12) and (20)) [Ns m^{-2}]
μ_a^f	fluid-phase apparent viscosity (Equation (19)) [Ns m^{-2}]
μ_r^f	fluid-phase *relative* viscosity (Equations (19) and (22))
ϕ	dependent variable in the general governing equation (Equation (1))
ϕ'	specularity factor (Equation (58))
Φ^s	dissipation function (Equation (11)) [W m^{-3}]
π	3.1415926
ρ	mass density in the general governing equation (Equation (1)) [kg m^{-3}]

Superscripts

f	pertaining to the fluid phase
int	pertaining to the fluid–solid interface
m	pertaining to the mass-flow related velocity
s	pertaining to the solid phase
*	pertaining to the previous time step

Subscripts

cv	pertaining to the control volume
ele	pertaining to the element
MX	related to maximum packing condition
o	pertaining to the centroid of the element
r	pertaining to the *r*-component equation or to point *r* (Figure 3)
s, *t*	pertaining to points *s* and *t*, respectively (Figure 3)
w	pertaining to values at the wall
z	pertaining to the *z*-component equation
ϕ	pertaining to the dependent variable

REFERENCES

1. C.T. Crowe, 'Review—numerical models for dilute gas–particle flows', *ASME J. Fluids Eng.*, **104**, 297–303 (1982).
2. C.T. Crowe, 'The state-of-the-art in the development of numerical models for dispersed phase flows', *Proc. Int. Conf. Multiphase Flows*, Tsukuba, Japan, 1991, pp. 49–60.
3. R. Ishii, Y. Umeda and M. Yuhi, 'Numerical analysis of gas–particle two-phase flows', *J. Fluid Mech.*, **203**, 475–515 (1989).

4. C.S. Campbell, 'Rapid granular flows', *Annu. Rev. Fluid Mech.*, **22**, 57–92 (1990).
5. S.B. Savage, 'Rheology of rapid granular flows: experiments, kinetic theory, computer simulations and some current issues', *Proc. Int. Conf. Multiphase Flows*, Tsukuba, Japan, 1991, pp. 109–125.
6. D. Gidaspow, 'Hydrodynamic modelling of circulating and bubbling fluidized beds', in M.C. Roco, (ed.), *Particulate Two-Phase Flow*, Butterworth-Heinemann, Boston, 1993, Chap. 22, pp. 778–810.
7. R. Jackson, 'The mechanics of fluidized beds', *Trans. Inst. Chem. Eng.*, **41**, 13–28 (1963).
8. S.L. Soo, *Fluid Dynamics of Multiphase Systems*, Blaisdell, Waltham, MA, 1967.
9. F.E. Marble, 'Dynamics of dusty gases', *Annu. Rev. Fluid Mech.*, **2**, 397–446 (1970).
10. S. Whitaker, 'The transport equations of multiphase systems', *Chem. Eng. Sci.*, **28**, 139–147 (1973).
11. C.T. Ishii, *Thermo-Fluid Dynamic Theory of Two-Phase Flow*, Eyrolles, Paris, 1975.
12. J.C. Slattery, *Momentum, Energy, and Mass Transfer in Continua*, Krieger, Malabar, 1981.
13. J.A. Bouré and J.M. Delhaye, 'General equations and two-phase flow modelling', in G. Hetsroni (ed.), *Handbook of Multiphase Systems*, Hemisphere Pub. Corp., Washington, 1982, Chap. 1, pp. 36–95.
14. D.A. Drew and R.T. Lahey, Jr., 'Analytical modelling of multiphase flow', in M.C. Roco (ed.), *Particulate Two-Phase Flow*, 1993, Chap. 16, pp. 509–566.
15. W.A. Sirignano, 'Fluid dynamics of sprays—1992 Freeman scholar lecture', *ASME J. Fluids Eng.*, **115**, 345–378 (1993).
16. O.R. Walton, 'Numerical simulation of inelastic, frictional particle–particle interactions', in M.C. Roco (ed.), *Particulate Two-Phase Flow*, Butterworth-Heinemann, Boston, 1993, Chap. 25, pp. 884–911.
17. J.A. Pita and S. Sundaresan, 'Gas–solid flow in vertical tubes', *AIChE J.*, **37**, 1009–1018 (1991).
18. J.A. Pita and S. Sundaresan, 'Developing flow of gas–particle mixture in a vertical riser', *AIChE J.*, **39**, 541–552 (1993).
19. J.A. Yasuna, H.R. Moyer, S. Elliot and J.L. Sinclair, 'Quantitative predictions of gas–particle flow in a vertical pipe with particle–particle interactions', *Power Technol.*, **84**, 23–34 (1995).
20. H.B. Stewart and B. Wendroff, 'Two-phase flow: models and methods', *J. Comput. Phys.*, **56**, 363–409 (1984).
21. A. Bedford and D.S. Drumheller, 'Theories of immiscible and structured mixture', *Int. J. Eng. Sci.*, **21**, 863–960 (1983).
22. T.B. Anderson and R. Jackson, 'A fluid mechanical description of fluidized beds', *I&EC Fundamentals*, **6**, 527–539 (1967).
23. J.D. Murray, 'On the mathematics of fluidization. Part 1. Fundamental equations and wave propagation', *J. Fluid Mech.*, **21**, 465–493 (1965).
24. R. Panton, 'Flow properties for the continuum viewpoint of a non-equilibrium gas–particle mixture', *J. Fluid Mech.*, **31**, 273–303 (1968).
25. Y.A. Buyevich, 'Statistical hydrodynamics of disperse systems. Part 1. Physical background and general equations', *J. Fluid Mech.*, **49**, 489–507 (1971).
26. J.C. Slattery, 'Flow of viscoelastic fluids through porous media', *AIChE J.*, **13**, 1066–1071 (1967).
27. S. Whitaker, 'Diffusion and dispersion in porous media', *AIChE J.*, **13**, 420–427 (1967).
28. D.A. Drew, 'Averaged field equations for two-phase media', *Stud. Appl. Math.*, **50**, 133–166 (1971).
29. G.H. Crapiste, E. Rotstein and S. Whitaker, 'General closure scheme for the method of volume averaging', *Chem. Eng. Sci.*, **41**, 227–235 (1986).
30. T.S. Jiang, M.H. Kim, V.J. Kremesee Jr., and J.C. Slattery, 'The local volume-averaging equations of motion for a suspension of non-neutrally buoyant spheres', *Chem. Eng. Commun.*, **50**, 1–30 (1987).
31. C.T. Crowe, M.P. Sharma and D.E. Stock, 'The particle-source-in cell (PSI-CELL) model for gas-droplet flows', *J. Fluids Eng.*, **99**, 325–332 (1977).
32. M. DiGiacinto, F. Sabetta and R. Piva, 'Two-way coupling effects in dilute gas–particle flows', *J. Fluid Eng.*, **104**, 304–312 (1982).
33. F. Durst, D. Milojevic and B. Schonung, 'Eulerian and Lagrangian predictions of particulate two-phase flows: a numerical study', *Appl. Math. Model.*, **8**, 101–115 (1984).
34. M.B. Carver, 'Numerical computation of phase separation in two fluid flow', *ASME J. Fluids Eng.*, **106**, 147–153 (1984).
35. F.H. Harlow and A.A. Amsden, 'Numerical calculation of multiphase fluid flow', *J. Comput. Phys.*, **17**, 19–52 (1975).
36. D.B. Spalding, 'Calculation of two dimensional two-phase flows', in F. Durst *et al.* (eds.), *Two Phase Momentum, Heat and Mass Transfer in Chemical Process, and Energy Engineering Systems*, Hemisphere, Washington D.C., 1979.
37. J.K. Dukowicz, 'A particle–fluid numerical model for liquid sprays', *J. Comput. Phys.*, **35**, 229–253 (1980).
38. S. Chapman and T.G. Cowling, *The Mathematical Theory of Non-Uniform Gases*, Cambridge University Press, Cambridge, 1939.
39. J.L. Sinclair and R. Jackson, 'Gas–particle flow in a vertical pipe with particle–particle interactions', *AIChE J.*, **35**, 1473–1486 (1989).
40. C.K.K. Lun, S.B. Savage, D.J. Jeffrey and N. Chepurniy, 'Kinetic theories for granular flow: inelastic particles in Couette flow and slightly inelastic particles in a general flowfield', *J. Fluid Mech.*, **140**, 223–256 (1984).
41. J. Ding and D. Gidaspow, 'A bubbling fluidization model using kinetic theory of granular flow', *AIChE J.*, **36**, 523–538 (1990).

42. C.K.K. Lun, 'Kinetic theories of granular flows', *Ph.D. Thesis*, Dept. of Civil Engineering, McGill University, Montreal, Canada, 1985.
43. P.C. Johnson and R. Jackson, 'Frictional-collisional constitutive relations for granular materials, with application to plane shearing', *J. Fluid Mech.*, **176**, 67–93 (1987).
44. P.R. Nott and J.F. Brady, 'Pressure-driven flow of suspensions: simulation and theory', *J. Fluid Mech.*, **275**, 157–199 (1994).
45. S.V. Patankar, *Numerical Heat Transfer and Fluid Flow*, McGraw-Hill, New-York, 1980.
46. C. Masson and B.R. Baliga, 'A control-volume finite element method for two-dimensional dilute fluid–solid particle flows', *Proc. First European Computational Fluid Dynamics Conference*, Brussels, Belgium, 1992, pp. 541–548.
47. C. Masson and B.R. Baliga, 'Computer simulation of axisymmetric dilute gas–solid particle flows in irregular geometries', *Gas–Solid Flows*, ASMEFED, **166**, 31–43 (1993).
48. C. Masson and B.R. Baliga, 'A control-volume finite element method for dilute gas–solid particle flows', *Comput. Fluids*, **23**, 1073–1096 (1994).
49. C. Masson, 'Numerical prediction of gas–solid particle flows over a wide range of concentration in irregular geometries', *Ph.D. Thesis*, Dept. of Mech. Eng., McGill University, Montreal, Canada, 1993.
50. J.H. Ferziger, 'Large eddy numerical simulations of turbulent flows', *AIAA J.*, **15**, 1261–1267 (1977).
51. J. Smagorinsky, 'General circulation experiments with the primitive equations: part I. The basic experiment', *Mon. Weather Rev.*, **91**, 99–164 (1963).
52. B.R. Baliga and S.V. Patankar, 'Elliptic systems: finite element method II', in W.J. Minkowycz *et al.* (eds.), *Handbook of Numerical Heat Transfer*, Wiley, New York, 1988, Chap. 11, pp. 421–461.
53. C. Prakash and S.V. Patankar, 'A control volume-based finite-element method for solving the Navier–Stokes equations using equal-order velocity–pressure interpolation', *Numer. Heat Transf.*, **8**, 259–280 (1985).
54. G.E. Schneider and M.J. Raw, 'A skewed positive influence coefficient upwinding procedure for control volume base finite element convection diffusion computation', *Numer. Heat Transf.*, **9**, 1–26 (1986).
55. G.E. Schneider and M.J. Raw, 'Control volume finite-element method for heat transfer and fluid flow using colocated variables—1. Computational procedure', *Numer. Heat Transf.*, **11**, 363–390 (1987).
56. C. Masson, H.J. Saabas and B.R. Baliga, 'Co-located equal-order control-volume finite element method for two-dimensional axisymmetric incompressible fluid flow', *Int. J. Numer. Methods Fluids*, **18**, 1–26 (1994).
57. H.J. Saabas and B.R. Baliga, 'Co-located equal-order control-volume finite-element method for multidimensional, incompressible, fluid flow—part I', *Numer. Heat Transf.*, **26B**, 381–407 (1994).
58. O.C. Zienkiewicz, *The Finite Element Method*, McGraw-Hill, London, 1977.
59. T.J. Barth, 'On unstructured grids and solvers', *Comput. Fluid Dynam., Von Karman Inst. Lect. Ser.*, 1990-03 (1990).
60. H.J. Saabas, 'A control volume finite element method for three-dimensional, incompressible, viscous fluid flow', *Ph.D. Thesis*, Dept. of Mech. Eng., McGill University, Montreal, Canada, 1991.
61. M. Peric, R. Kessler and G. Scheuerer, 'Comparison of finite volume numerical methods with staggered and co-located grids', *Comput. Fluids*, **16**, 389–403 (1988).
62. J.G. Rice and R.J. Schnipke, 'An equal-order velocity–pressure formulation that does not exhibit spurious pressure modes', *Comp. Methods Appl. Mech. Eng.*, **58**, 135–149 (1986).
63. C.M. Rhie and W.L. Chow, 'Numerical study of the turbulent flow past an airfoil with trailing edge separation', *AIAA J.*, **21**, 1525–1532 (1983).
64. K. Hui, P.K. Haff, J.E. Ungar and J. Jackson, 'Boundary conditions for high-shear grain flows', *J. Fluid Mech.*, **145**, 223–233 (1984).
65. D. Leighton and A. Acrivos, 'The shear induced migration of particles in concentrated suspensions', *J. Fluid Mech.*, **181**, 415–439 (1987).
66. P. Hookham, 'Concentration and velocity measurements in suspensions flowing through a rectangular channel', *Ph.D. Thesis*, California Institute of Technology, Pasadena, USA, 1986.
67. S.B. Savage and M. Sayed, 'Stresses developed by dry cohesionless granular materials sheared in an annular shear cell', *J. Fluid Mech.*, **142**, 391–430 (1984).
68. D.M. Hanes and D.L. Inman, 'Observations of rapidly flowing granular fluid materials, *J. Fluid Mech.*, **150**, 357–380 (1985).
69. C.K.K. Lun and S.B. Savage, 'A simple kinetic theory for granular flow of rough, inelastic, spherical particles', *J. Appl. Mech.*, **54**, 47–53 (1987).

